



**POLITECNICO  
DI TORINO**



## MASTER'S THESIS

Master of Science in NANOTECHNOLOGIES FOR ICTs

Academic Year 2017/18

---

# Extracting the penetration depth from the critical current of superconducting microbridges

---

*Author:*

Luca CAMELLINI

*Supervisor:*

Prof. Renato GONNELLI

*Co-supervisor:*

Dr. Matteo COCUZZA

*Advisor:*

Prof. Karl K. BERGGREN



**Massachusetts  
Institute of  
Technology**

*Quantum Nanostructures and Nanofabrication Group*

*Massachusetts Institute of Technology*



# *Abstract*

## **Extracting the penetration depth from the critical current of superconducting microbridges**

by Luca CAMELLINI

The penetration depth of a superconductor accounts for how the magnetic field is screened by the material. It is also linked to the kinetic inductance, which is of critical importance in the design of detectors and electrical circuits.

This work presents a novel method for an indirect measurement of the penetration depth which requires the fabrication of microbridges with standard electron beam lithography processes, similar to those employed for detectors, and DC measurements without any external applied magnetic field. It is in fact possible to extract the value of the penetration depth by measuring the critical current of bridges with a range of widths up to a few times the Pearl length, and comparing it with the current distribution given by London equations, obtained with a finite element model.

Niobium nitride was the material of choice in this work, deposited via reactive DC magnetron sputtering at room temperature, and a layout optimization process was applied to decrease current crowding effects. A process for the fabrication of the bridges was devised: gold electrical contact pads were patterned first with direct write lithography, followed by e-beam evaporation of the metal and bi-layer lift-off; microbridges were patterned with electron beam lithography, then etched with RIE.

Results from measurements performed with a cryogenic probe station at a temperature of 4.8 K, provided a value of the London depth between 389 and 457 nm, and a critical current density compatible with values reported in literature and independently measured. The temperature dependence of the critical current was also investigated.

## *Résumé*

### **Extraire la profondeur de pénétration du courant critique de micro-ponts supraconducteurs**

par Luca CAMELLINI

La longueur de pénétration de London d'un supraconducteur est une propriété matérielle expliquant comment le champ magnétique est filtré par un supraconducteur. Il est également lié à l'inductance cinétique, qui est d'une importance critique dans la conception des détecteurs et circuits électriques.

Ce travail présente une nouvelle méthode pour une mesure indirecte de la longueur de pénétration qui nécessite la fabrication de micro-ponts par lithographie à faisceau d'électrons et les mesures en courant continu sans aucun champ magnétique externe appliqué. Il est en fait possible d'extraire la valeur de la longueur de pénétration en mesurant le courant critique des ponts qui ont une gamme de largeurs allant jusqu'à quelques fois la longueur de Pearl, et en le comparant avec la distribution du courant donnée par les équations de London, obtenues avec un modèle d'éléments finis.

Le nitrure de niobium était le matériau de choix dans ce travail, déposé par réaction par pulvérisation magnétron à courant continu à température ambiante et une démarche d'optimisation de la disposition a été appliqué pour diminuer les effets d'accumulation de courant. Nous avons conçu un processus pour la fabrication des ponts: les plots de contact électriques en or ont été façonné par écriture lithographique directe; les micro-ponts ont été modelées avec une lithographie par faisceau d'électrons, puis gravées par gravure ionique réactive.

Les résultats de mesures effectuées avec une station de sonde cryogénique à une température de 4,8 K, ont montré que la profondeur de London comprise entre 389 et 457 nm, et une densité de courant critique compatible avec les valeurs rapportées dans la littérature et indépendamment mesuré. La dépendance en température du courant critique était également étudiée.

# *Sintesi*

## **Estrazione della lunghezza di penetrazione dalla corrente critica di microbridge superconduttore**

di Luca CAMELLINI

La lunghezza di penetrazione di un superconduttore è una proprietà che descrive come il campo magnetico viene espulso dal materiale. È anche legata all'induttanza cinetica, di importanza critica nel design di fotorivelatori e circuiti elettronici.

Questo lavoro presenta un nuovo metodo per una misurazione indiretta della lunghezza di penetrazione che richiede la fabbricazione di microbridge con processi standard di litografia a fasci di elettroni, simili a quelli utilizzati per i rivelatori, e misure in corrente continua senza campi magnetici esterni. Infatti, è possibile estrarre la lunghezza di penetrazione misurando la corrente critica di microbridge di larghezza variabile fino ad alcune volte la lunghezza di Pearl, e comparandola con la distribuzione di corrente data dalle equazioni di London, risolte tramite un modello a elementi finiti.

Il materiale utilizzato in questo lavoro è stato il nitrato di niobio, depositato tramite DC magnetron sputtering reattivo a temperatura ambiente, e un processo di ottimizzazione del layout dei dispositivi è stato applicato per ridurre gli effetti di current crowding. È stato ideato un processo di fabbricazione dei microbridge, in cui i contatti elettrici sono stati creati tramite litografia direct write e lift-off, mentre i dispositivi sono stati ottenuti tramite litografia elettronica e reactive ion etching.

È stato individuato un valore per la lunghezza di penetrazione compreso tra 389 e 457 nm, ottenuto da misure in una stazione a sonda meccanica criogenica a una temperatura di 4.8 K, e una densità di corrente critica compatibile con quanto riportato in letteratura e misurato indipendentemente. Inoltre, è stata analizzata la dipendenza della corrente critica dalla temperatura.



## *Acknowledgements*

This thesis is the result of a two-year journey which has revealed to be full of obstacles but very rewarding. A heartfelt thank you goes to every person that walked with me on this incredible road.

I would like to thank my advisor, Prof. Karl K. Berggren, who gave me the opportunity of joining the QNN group and provided guidance throughout the whole project. Several people helped me along the way; Dr. Reza Baghdadi with constant mentorship, Di Zhu with the theoretical model, Marco Colangelo with his fab knowledge and a great deal of patience, and Owen Medeiros with his mastery of the film deposition and characterization techniques. Without all these people, this work would have never been written.

My appreciation goes as well to Jim Daley and Mark Mondol for the help in the nanofabrication processes, and to all of the people in the QNN group for the cheerful moments spent together.

A big thank you to my friends and family, particularly my mother, who always relentlessly supported me, and to my Nanotech colleagues, the extraordinary people who became my family for the last two years. A final thought of enormous gratitude is for my late grandparent Donato, my first supporter and teacher.



# Contents

<b>Abstract</b>	<b>iii</b>
<b>Acknowledgements</b>	<b>vii</b>
<b>Contents</b>	<b>ix</b>
<b>1 Introduction</b>	<b>1</b>
1.1 Superconductivity . . . . .	1
1.2 London theory . . . . .	2
1.3 Kinetic inductance . . . . .	4
1.4 Penetration length measurement techniques . . . . .	6
1.5 Critical current . . . . .	7
1.6 Objective . . . . .	9
<b>2 Model</b>	<b>11</b>
2.1 Current distribution in superconducting thin films . . . . .	11
2.2 Finite element model . . . . .	12
2.3 $\lambda$ dependence on the local current density . . . . .	16
<b>3 Design and fabrication process</b>	<b>19</b>
3.1 Thin film deposition and characterization . . . . .	19
3.2 Chip layout design . . . . .	22
3.3 Fabrication process . . . . .	25
3.3.1 Electrical contact pads . . . . .	25
3.3.2 Microbridges patterning . . . . .	28
3.3.3 Process enhancement . . . . .	33
<b>4 Experimental results and discussion</b>	<b>37</b>
4.1 Measurement setup . . . . .	37
4.2 Measurements at 4 K . . . . .	39
4.2.1 Cryogenic system . . . . .	39
4.2.2 Results . . . . .	42
4.2.3 Data fitting . . . . .	42
4.2.4 Film aging . . . . .	45
4.3 Temperature dependence . . . . .	46
<b>5 Conclusions and future works</b>	<b>49</b>
<b>Bibliography</b>	<b>51</b>



# List of Symbols

$\lambda_L, \lambda$	London penetration depth	m
$\Lambda$	Pearl length, two-dimensional screening length	m
$\xi$	Superconducting coherence length	m
$H_c$	Critical magnetic field in type-I superconductors	$A \times m$
$H_{c1}, H_{c2}$	Lower and upper critical magnetic field in type-II superconductors	$A \times m$
$T_c$	Critical temperature, superconducting transition temperature	K
$J_c$	Critical current density	$MA \text{ cm}^{-2}$
$I_c$	Critical current	A
$L_k$	Kinetic inductance	H
$\mathcal{L}_k$	Kinetic inductivity	$H \text{ m}^{-2}$
$t$	Thickness, bridge cross section	m
$w$	Width, bridge cross section	m



## Chapter 1

# Introduction

### 1.1 Superconductivity

If the reader was to have a piece of metal such as lead or niobium, and to send a current through it, they would start feeling it getting warm, due to dissipation induced by the Joule effect: the passage of electric current through a conductor produces heat. If that same piece of metal was instead placed in a very good cooler, able to reach temperatures in the order of a few degrees Kelvin, they would notice that the metal conducts current without any dissipation.

This effect is one of the two macroscopic phenomena that describe superconductivity, a property of some materials that was discovered in 1911 by H. Kamerlingh Onnes [1]. When various metals are brought to temperatures below a critical value  $T_c$  – usually less than 10 K – their electrical resistance disappears completely: if a current is induced in a closed superconducting loop, that current would flow indefinitely.

The second property of this peculiar class of materials was discovered in 1933 by Meissner and Ochsenfeld [2], who found that not only a magnetic field can not penetrate inside a superconductor, but also that any magnetic field that is present in the material is expelled from it as soon as its temperature goes below  $T_c$ . The existence of this effect also implies the presence of a critical magnetic field  $H_c$  above which superconductivity is destroyed.

## 1.2 London theory

The first theoretical explanation of superconductivity was developed by the London brothers, Fritz and Heinz, in 1935 [3]. Their models explain the two basic yet peculiar phenomena of superconductivity that we mentioned before: perfect conductivity and the expulsion of magnetic fields.

The model can be summed up in two equations, from now on called the London equations:

$$\frac{\partial}{\partial t} \mathbf{J}_s = \frac{n_s e^2}{m_e} \mathbf{E} \quad (1.1)$$

$$\nabla \times \mathbf{J}_s = -\frac{n_s e^2}{m_e} \mathbf{B} \quad (1.2)$$

where  $n_s$  is the density of *superelectrons*, and  $m_e$  and  $e$  are the electron rest mass and charge, respectively. Equation 1.1 replaces Ohm's law inside a superconductor and is an *acceleration equation*, and describes perfect conductivity [4, p. 4]

Equation 1.2 can be combined with Maxwell's equation for the stationary case  $\nabla \times \mathbf{B} = \mu_0 \mathbf{J}$ , leading to

$$\nabla^2 \mathbf{B} = \frac{1}{\lambda_L^2} \mathbf{B} \quad (1.3)$$

with

$$\lambda_L = \sqrt{\frac{m_e \mu}{n_s e^2}} \quad (1.4)$$

being the London penetration depth ( $\mu$  is the magnetic permeability). It can be easily shown that  $\lambda$  represents the characteristic length of penetration of a magnetic field inside a superconductor [5, p. 62]; if we consider a superconductor whose surface lies on the  $y$ - $z$  plane, and a magnetic field  $\mathbf{B} = B_z \hat{\mathbf{z}}$  is applied, equation 1.3 is reduced to  $\frac{d^2}{dx^2} B_z = \frac{1}{\lambda^2} B_z$ , whose solution is

$$B_z(x) = B_0 \exp\left(-\frac{x}{\lambda}\right) \quad (1.5)$$

where  $x$  is the depth inside the superconductor.

The two London equations 1.1, 1.2 can be combined in a single equation expressed in terms of the magnetic vector potential  $\mathbf{A}$ , defined as  $\mathbf{B} = \nabla \times \mathbf{A}$ :

$$\mathbf{J}_s = -\frac{n_s e^2}{m_e} \mathbf{A} \quad (1.6)$$

which holds true if the gauge for the vector potential is chosen in a way that satisfies the condition  $\nabla \cdot \mathbf{A} = 0$ , called the London gauge. Equation 1.1 can then be retrieved by taking the time derivative on both sides, while 1.2 is obtained by taking the curl. It is also worth noticing that the proportionality constant is linked to  $\lambda$  by  $\frac{n_s e^2}{m_e} = \frac{\mu}{\lambda_L^2}$ .

It can also be shown [3] that Eq. 1.3 holds true for the 10 quantities  $\mathbf{B}, \mathbf{A}, \mathbf{J}_s, \rho$ :

$$\left\{ \begin{array}{l} \nabla^2 \mathbf{B} = \frac{1}{\lambda_L^2} \mathbf{B} \\ \nabla^2 \mathbf{A} = \frac{1}{\lambda_L^2} \mathbf{A} \\ \nabla^2 \mathbf{J}_s = \frac{1}{\lambda_L^2} \mathbf{J}_s \\ \nabla^2 \rho = \frac{1}{\lambda_L^2} \rho \end{array} \right. \quad (1.7)$$

Finally, equation 1.4 defines the density of superelectrons  $n_s$  as only dependent on universal constants and  $\lambda_L$ , a measurable quantity whose evaluation is the scope of the work here presented. The value of  $n_s$  varies continuously from a maximum value at zero kelvin, to zero at temperatures equal or above the phase transition temperature from the superconducting to normal state, also known as critical temperature  $T_c$ . The exact temperature dependence of  $\lambda_L$  is accounted for by the microscopic theory of superconductivity – also known as BCS theory –, but it is frequently assumed [4, p. 19] that the penetration depth roughly varies with the temperature as

$$\lambda_L(T) \approx \lambda_L(0) \sqrt{\frac{1}{1 - \left(\frac{T}{T_c}\right)^4}} \quad (1.8)$$

## Pearl length

The exponential decay of a magnetic field holds true for a bulk superconductor, but things become very different in the case of structures in which one or more dimensions are confined. In the case of thin films ( $d/\lambda \ll 1$ , where  $d$  is the thickness) the

current density  $\mathbf{j}$  can be represented [6] as a current sheet

$$\mathbf{j} = \mathbf{K}\delta(z) \quad (1.9)$$

and the London equation 1.7 can be rewritten as

$$\nabla^2 \mathbf{A} = \frac{d}{\lambda^2} \mathbf{A}\delta(z) \quad (1.10)$$

One can thus define a new length in thin films, from now on called the Pearl length, as

$$\Lambda = \frac{\lambda^2}{d} \quad (1.11)$$

which effectively represents the two-dimensional screening length in thin films.

### 1.3 Kinetic inductance

The first London equation, eq. 1.1, establishes a proportionality between the time derivative of a current and the electric field in a superconductor, which is effectively an inductor constitutive relation of the type

$$V = -L \frac{\partial I}{\partial t} \quad (1.12)$$

It is possible to better visualize the inductive behaviour of a superconductor making use of the Drude classical conductivity model [5, p. 15], which provides a linear relationship between the current density and the electric field in a material

$$\mathbf{j} = \sigma \mathbf{E} \quad (1.13)$$

defining the conductivity as

$$\sigma = \frac{ne^2}{m} \tau \quad (1.14)$$

where  $\tau$  is the average time between electron scattering events. This expression can be easily generalized to the AC case [7].

Let us rewrite eq. 1.13 with the complex representation for the AC case

$$\mathbf{j}e^{-i\omega t} = \sigma(\omega)\mathbf{E}e^{-i\omega t} \quad (1.15)$$

and in order to obtain the expression for  $\sigma(\omega)$  at finite frequencies, we introduce the equation of motion of an electron subject to scattering

$$\frac{d\mathbf{p}(t)}{dt} = -\frac{\mathbf{p}(t)}{\tau} + e\mathbf{E}(t) \quad (1.16)$$

Equation 1.3 can be expressed in the frequency domain, and by using the definition of current density

$$\mathbf{j}(\omega) = -\frac{ne\mathbf{p}(\omega)}{m} \quad (1.17)$$

the conductivity expression for a finite frequency  $\omega$  is retrieved as

$$\sigma(\omega) = \frac{ne^2}{m} \frac{1}{\tau^{-1} - i\omega} \quad (1.18)$$

The integral of the real part of eq. 1.18 is a finite value independent of  $\tau$

$$\int_{-\infty}^{\infty} \text{Re}[\sigma(\omega)]d\omega = \frac{\pi ne^2}{m} \quad (1.19)$$

while the limit for  $\tau \rightarrow \infty$  (perfect conductor) results in an imaginary value

$$\lim_{\tau \rightarrow \infty} \sigma(\omega) = -\frac{ne^2}{i\omega m} \quad (1.20)$$

The overall frequency behaviour in the London model of the superconductor is thus given by

$$\sigma(\omega) = \frac{\pi n_s e^2}{m_e} \delta(\omega) - \frac{n_s e^2}{i\omega m_e} \quad (1.21)$$

which corresponds to a purely inductive response for frequencies  $\omega \neq 0$ .

While in resistive wires the inductance mostly arises from the energy stored in the magnetic field (magnetic self-inductance), in a superconductor it is largely dominated by the *kinetic inductance*, linked to the energy of the motion of charge carriers (i.e. Cooper pairs). The impedance of a superconductor, thanks to the absence of a

resistive behaviour, is thus entirely due to its kinetic inductive component [8].

By recalling the definition of the London penetration depth from eq. 1.4, the frequency-dependent conductivity of eq. 1.21 can be rewritten as [9]:

$$\sigma(\omega) = \frac{1}{\mu_0 \lambda_L^2} \left[ -\frac{i}{\omega} + \pi \delta(\omega) \right] \quad (1.22)$$

which makes explicit the dependence of the kinetic inductance from the penetration length  $\lambda_L$ . We can now define the kinetic inductivity  $\mathcal{L}_K$  by rewriting the imaginary part of the conductance as impedance:

$$z(\omega) = i \frac{m\omega}{ne^2} = i\omega \mu_0 \lambda_L^2 = i\omega \mathcal{L}_K \quad (1.23)$$

The kinetic inductance of a superconductor is a fundamental property that is exploited in the design of superconducting circuits [10] and detectors [11]. In particular, it is directly related to the reset time of superconducting nanowire single photon detectors [12].

By exploiting the nonlinearity of the kinetic inductance on the current (which we will show in detail in section 2.3), several devices have been proposed such as high-temperature superconducting photomixers [13], where a local drop in the superelectron density generates a voltage due to the acceleration of the remaining carriers, ultrafast photokinetic samplers [14], amplifiers [15], and magnetometers [16]. Other studies utilized the kinetic inductance of the superconductor to create lumped element resonant circuits that can act as detectors [17] or galvanometers [18].

## 1.4 Penetration length measurement techniques

So far, we have shown the meaning of the London penetration length, how it describes the behaviour of superconductors both in bulk and thin films, and its link with the kinetic inductance. We now present several methods of direct and indirect measurements for  $\lambda$ .

Several methods have been demonstrated: one of the most direct is to measure the diamagnetic response of the superconductor. This can be achieved with DC magnetic susceptibility measurements performed with SQUID magnetometers, where

variations of  $\lambda$  with temperature are linked to variation in the magnetic susceptibility by  $\Delta\chi/\chi_0 = 2\Delta\lambda/d$ , while the value of  $\lambda_0$  (the penetration depth at zero temperature) is extracted by using the known temperature dependence of  $\lambda$  from eq. 1.2. This type of measurement provides the best results for single-crystal materials [19]. AC magnetic susceptibility measurements can also be employed, where the magnetic moment of the film is measured in an applied alternating magnetic field at kilohertz frequencies [20].

Moreover, numerous high frequency types of measurement can be employed, such as THz pulse spectroscopy, where a pulse is sent through the sample and is reshaped according to the kinetic inductance of the superconductor [9]. Other techniques based on the inductive behaviour of superconductors exploit the  $\lambda$ -dependence of the propagation velocity of EM waves in transmission lines [21], or the change of resonant frequency in lumped resonant circuits where the inductor is a microstrip [22] or nanowire [8] resonator, according to

$$f_{res} = \frac{1}{2\pi\sqrt{L_K C}} \quad (1.24)$$

All the mentioned techniques allow for penetration depth measurements with variable precision and noise levels; nevertheless, all the methods available for thin films require either the design and fabrication of a full device or circuit, RF measurements, or the use of external variable magnetic fields.

## 1.5 Critical current

There is a limit to the total current that can flow through superconductor before it becomes resistive, which is the *critical current*. The physical phenomenon causing the transition depends on the sample dimensions, the characteristics of the material and whether it is a type-I or type-II superconductor. In the latter case, vortex penetration at high current has to be taken into account.

The ultimate maximum is the *depairing current*, that occurs when superelectrons reach a threshold velocity above which the superconducting gap goes to zero: at this

point, excitations can happen at zero energy and dissipation occurs [23]. Nevertheless, in the case of a superconducting microbridge, this value can only be reached when its width is both smaller than  $\lambda_p$  and  $4.4\zeta$  [24]. Since the coherence length in niobium nitride – material of choice in this work as detailed in section 3.1 – is lower than 5 nm [25], the dimensions of the bridges employed in this work are always above this limit.

If the width of the wire is larger than  $4.4\zeta$ , the critical current is due to vortex penetration at the edges, occurring when the self-field generated by the applied current reaches the barrier penetration field. This value usually corresponds to the lower critical field but, in the presence of a Bean-Livingston barrier [26] the value can raise up to the thermodynamic critical field  $H_{c2}$  [27].

A three-current model for the maximum dissipation-free current in a superconductor is usually considered [28, 29], with two different critical current densities in addition to the depairing current density. The first one is that required for the penetration of vortices  $j_{pen}$ , the second is the depinning current  $j_{pin}$  at which vortices start moving towards the centre of the strip subject to a Lorentz force [30]. While  $j_{pen}$  is a geometry-dependent property,  $j_{pin}$  is linked to pinning centers and is thus a material property. In some cases, the penetration of vortices causes the onset of dissipation, while in others vortices can remain pinned on pinning sites close to the edge of the bridge until the current is further increased. It has been demonstrated [31] the opportunity of nanoengineering materials in order to create artificial pinning sites and reaching the depairing current.

The critical current density in type-II superconductors is thus presumed to be governed by vortex penetration and flux pinning [32]. Nevertheless, a recent work [33] on Hall measurements of the magnetic field in superconducting tape at the critical state showed how the distribution of the field fits a model with a uniform current distribution, instead of the one suggested by Rhoderick and Wilson [34] (assessed in section 2.1) which only holds at values of current that are below the critical one. Increasing the current, according to the authors, moves the current distribution from London equations-driven to uniform in a continuous manner.

Another analysis by Talantsev et al. [35], which included several materials, showed that the critical current density has a universal scaling law and that in the case of thin

films (thickness much lower than the penetration depth) the current distribution can always be assumed uniform, independently of the aspect ratio of the bridge. For thin type-II superconducting films, a normalized critical surface current density can be defined as

$$J_s^n = J_c \times \frac{b/\lambda}{\tanh b/\lambda} \frac{4\pi\mu_0\lambda^3}{\phi_0(\ln \kappa + 0.5)} \quad (1.25)$$

with  $b$  being the thickness,  $k = \lambda/\xi$ , and this normalized value was shown to be always around 1 for  $b \ll \lambda$ , which means the critical current is entirely due to self-field effects. Although this analysis sounds promising, we were not able to match the results of this work using values of critical currents for different widths on NbN thin films reported elsewhere [28].

In the scope of this work, we assume that the critical current density is a property linked to the material and independent of geometry, and we assume that the current distribution follows London equations as the model described by Rhoderick and Wilson.

## 1.6 Objective

The work presented here aims at the measurement of the critical current of niobium nitride microbridges with widths both smaller and larger than the two-dimensional screening length  $\Lambda$  in order to extract a value for the penetration depth. Chapter 2 presents the current distribution model employed, obtained by solving London equations with a finite element analysis. In chapter 3 we show the deposition process for NbN, the methods for characterizing superconducting thin films, and the fabrication process for microbridges by electron beam lithography. Finally, chapter 4 addresses the cryogenic measurement setup, with a discussion of the results of critical current measurements, as well as temperature dependence measurements and film aging concerns. We compare in this chapter the results we obtained to the model presented in chapter 2 to extract a value for the Pearl length of the superconducting film.



## Chapter 2

# Model

When a current is sent through a superconductor, it tends to flow on the outer surface of the material, with a characteristic length driven by the London parameter in the case of bulk superconductors, or the Pearl length in thin films. In this chapter, we show the theoretical models for the current distribution in thin superconducting films with a rectangular cross section, and we compare them with the results of a finite element analysis. Moreover, we apply the finite element method to predict critical current values as a function of the width of a microbridge.

### 2.1 Current distribution in superconducting thin films

The most simple model for a superconducting microbridge is given by a two-dimensional problem of a thin film of constant cross-section and infinite length. The current and magnetic field distribution inside such a structure can be obtained by solving London's equations with appropriate boundary conditions [36].

The problem of the current distribution inside a superconducting film has been studied in detail by several authors, and a first approximate solution for the case of thickness  $t \leq \lambda$  was provided by Marcus, 1961 [37]:

$$\begin{aligned}
 J(s) &= 1 + \int_0^1 J(s')K(s,s')ds', \quad s = \frac{2x}{w} \\
 K(s,s') &= \frac{\beta^2 wt}{16\pi} \left[ M\left(\frac{w}{t}(s-s')\right) + M\left(\frac{w}{t}(s+s')\right) \right] \\
 M(u) &= 2 \ln(1+u^2) - 4 + 4u \arctan u^{-1}, \quad u \geq 0
 \end{aligned} \tag{2.1}$$

The solution only depends on the  $x$  coordinate, because the current is assumed uniform along the thickness, being it smaller than the penetration depth [6]. Equation 2.1 is a Fredholm equation of the second kind; it can be solved numerically with the methods identified by Rahbar and Hashemizadeh [38].

W.A. Bowers (unpublished, cited by Glover [39]) provided an approximate analytical solution to the current in a superconducting slab, in the case of thickness comparable with the penetration depth and width much greater, such that  $wd \gg \lambda^2$ , or equivalently  $w \ll \Lambda$ :

$$J(x) = J(0) \left[ 1 - \left( \frac{2x}{w} \right)^2 \right]^{-1/2} \quad (2.2)$$

where  $x$  is the distance from the centre of the slab. This solution diverges at  $x = w$ . Rhoderick and Wilson [34] showed that near the edge the solution has the form

$$J(x) = J\left(\frac{w}{2}\right) \exp \left[ -\frac{d \left( \frac{w}{2} - x \right)}{a\lambda^2} \right] \quad (2.3)$$

where  $a$  is a constant of order unity, and usually chosen as 1 or 2. The two solutions (Eq. 2.2 and 2.3) are joined at a point distant

$$\frac{a\lambda^2}{2d} \quad (2.4)$$

from the edge of the film.

## 2.2 Finite element model

The same problem was solved numerically with the aid of a finite element tool, COMSOL Multiphysics 5.3a. We used the Helmholtz Equation physics, from the Mathematics module. We considered a cross section of the wire perpendicular to the direction of the current, and modelled the problem as follows:

- An inner box, representing the wire cross section, inside of which we solved for  $\nabla^2 \mathbf{A} = \frac{1}{\lambda_L^2} \mathbf{A}$  (eq. 1.7), and whose dimensions correspond to the width and thickness of the wire,
- an outer box, much larger than the inner one, representing the dielectric surrounding the wire, where we solved for  $\nabla^2 \mathbf{A} = 0$ , from Maxwell's equations.

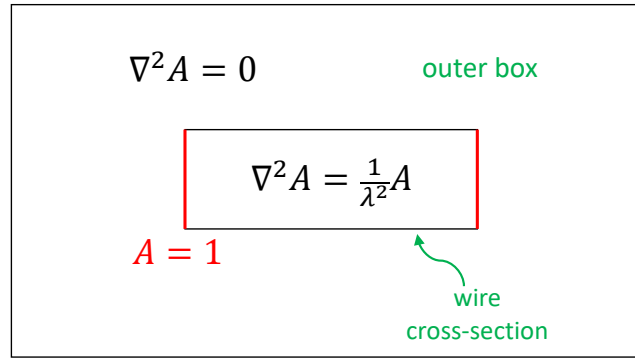


FIGURE 2.1: Schematics of the model employed, which is a representation of the microbridge cross-section. We solved for London equation inside the superconductor and for Laplace equation in the surrounding area. The vector potential value is fixed to 1 at the edges of the wire, where it is assumed to be maximum.

We also set the value of the vector potential on the sides of the bridge – where it reaches its maximum value – arbitrarily to 1, and a boundary condition of zero flux (the spatial derivative of the vector potential is null) was applied at the edges of the outer box. A schematic representation is given in figure 2.1.

The analysis provides the distribution of the magnetic vector potential inside the wire, which has a direct proportionality (see eq. 1.6) with the current density.

### Mesh

The inner box was divided in several rectangular domains along the width, while one single domain was placed along the thickness. This is in accordance with the hypothesis we previously made, that  $t \ll \lambda$  and thus no significant variation of the current density occurs along the thickness of the wire.

An intermediate domain was added as an interface between the wire and the external box, to allow for a much less refined mesh in the outer region – thus significantly reducing the computation time – while keeping the wire and its surrounding region finely meshed (around 2000 domains, depending on the wire width).

### Results

Fixing the thickness of the wire, a parametric sweep was performed, obtaining the current density distribution for widths ranging from 1 to 105  $\mu\text{m}$ . We present all the

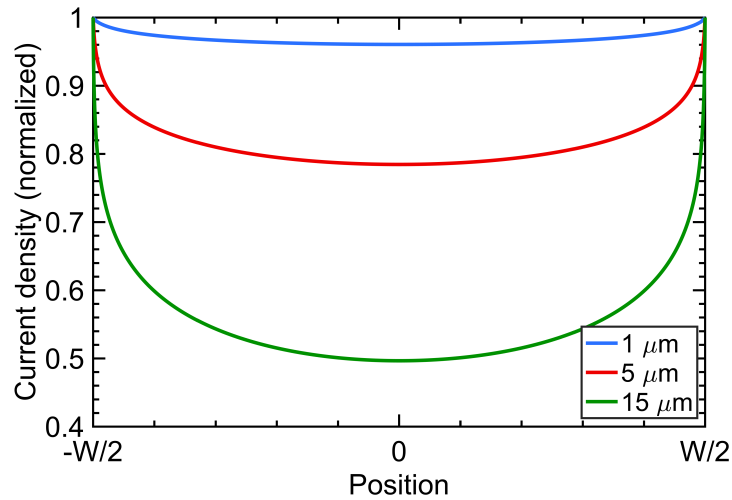


FIGURE 2.2: Current distribution in a microbridge according to London equation, for different widths. For small wires, the magnetic field can penetrate and the current distribution is almost uniform; the distribution becomes more and more peaked at the edges as the width is increased above the 2-dimensional screening length  $\Lambda$ .

results for a thickness of 20 nm unless otherwise specified. Figure 2.2 shows the current density distribution, normalized to the width, for a fixed value of  $\lambda$  and various widths. As expected, as the width becomes larger the distribution becomes sharply peaked at the edges of the wire, meaning that most of the current is flowing in the outer region.

It is worth noticing that, while several authors [28, 40, 41] consider the Pearl length a limit under which the distribution is uniform, that is not likely the case, and even at widths equal to one tenth of the Pearl length the current at the center is only 96% its maximum value.

The distributions from figure 2.2 can be integrated along the width of the microbridge to obtain the total current as a function of the width, assuming a constant value for the edge current density. The results are shown in figure 2.3 for different values of the Pearl length  $\Lambda$ . In narrow bridges, the current follows an approximately linear trend, while at larger widths a saturation regime is reached, due to the current flowing almost entirely at the edges. The total maximum current that can be carried by the wire, as well as width for the onset of saturation, strictly depend on  $\Lambda$ : lower values of the Pearl length correspond to a lower maximum current, and saturation is reached at smaller dimensions.

Figure 2.4 also shows the *reduction factor*, representing the ratio between the total

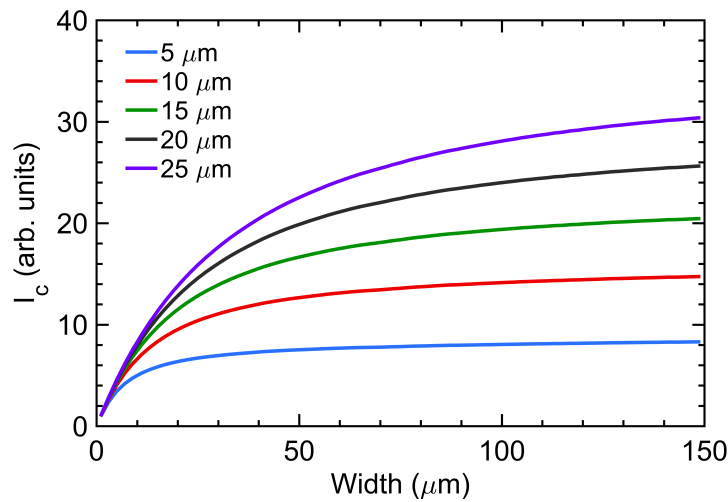


FIGURE 2.3: Integrated current distribution as a function of the bridge width for different values of Pearl length, from  $5 \mu\text{m}$  (blue) to  $25 \mu\text{m}$  (purple). The current density at the edges is fixed to an arbitrary unitary value. Lower values of  $\Lambda$  show a saturation of the integrated current at high widths, due to the current concentrating at the edges of the wire.

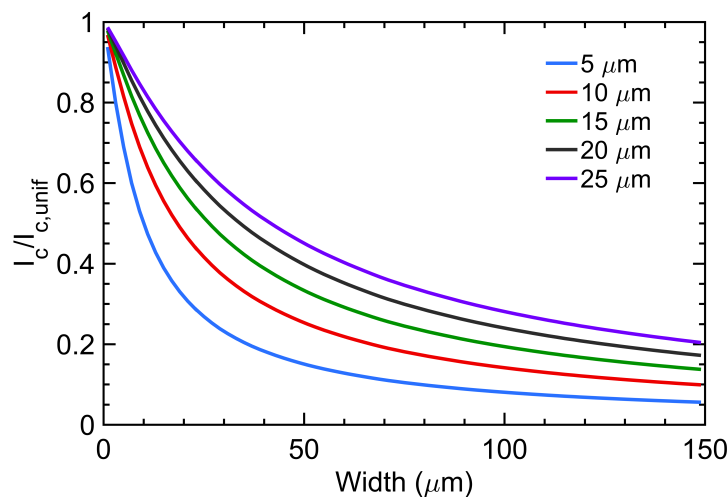


FIGURE 2.4: *Reduction factor* computing by dividing the integrated values in figure 2.3 by the width of the wire. It represent how the current is reduced due its distribution following London equations, with respect to the current the wire would carry in the case of uniform current distribution.

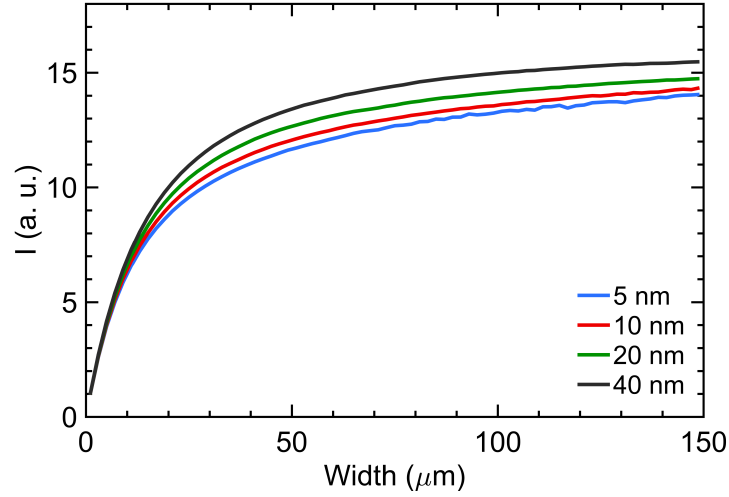


FIGURE 2.5: Results of the FEM solution for  $\Lambda = 8 \mu\text{m}$  and thickness of the film ranging from 5 to 40 nm. Results are consistently similar (within 5 % for the thinnest bridges), while they start to deviate at larger thickness, due to the condition  $t \ll \lambda$  not being satisfied anymore. 40 nm for instance is only 12 times smaller than  $\lambda$ .

current in a wire where the current distribution is uniform compared to the one obtained from solving London's equations. It represents the difference from the linear regime, and these values will be used in section 4.2.3 to fit the experimental data to the model.

One final result that can be obtained from this finite element analysis is a confirmation of Pearl's theory: the current distribution in a thin film depends uniquely on the width of the film and on the value of  $\Lambda$ , and is independent of the thickness. Figure 2.5 displays the current distribution for different values of thickness, keeping the width and Pearl length constant. It is possible to observe that the differences are minimal when in the limit of  $t \ll \lambda$ .

### 2.3 $\lambda$ dependence on the local current density

So far we have considered  $\lambda$  as a constant parameter: recalling equation 1.4, we can see that it depends on some physical constants and on  $n_s$ , the density of superelectrons (Cooper pairs). While this value is linked to material properties, it is also influenced by the current flowing in the superconductor; a higher current density leads to a lower number of superelectrons, eventually going to zero once the critical current is reached.

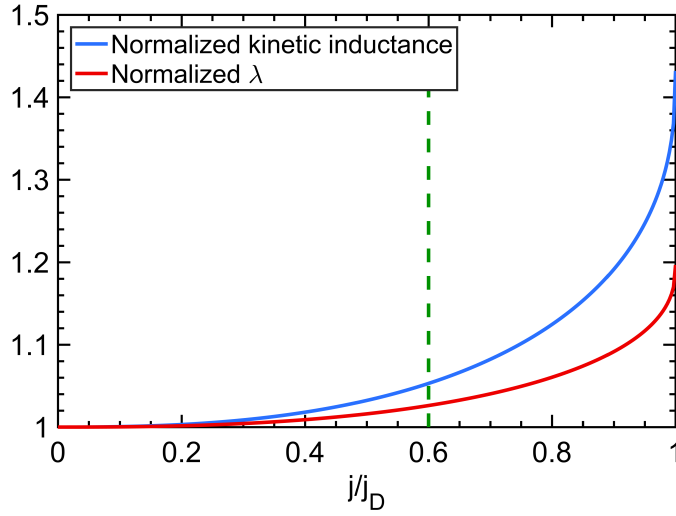


FIGURE 2.6: Relative increase in kinetic inductivity  $\mathcal{L}_k$  (blue) and penetration depth  $\lambda$  (red) as a function of the current density for  $T = \frac{T_c}{2}$  as reported from [40]. The green vertical dashed line shows the value of the switching current with respect to the depairing current, from [42].

Clem and Kogan[40] reported the dependence on the kinetic inductance on all ranges of current densities up to the depairing current:

$$\frac{\mathcal{L}_k(x)}{\mathcal{L}_{k,0}} = y_0 - (y_0 - 1)(1 - x^n)^{\frac{1}{n}} \quad (2.5)$$

where  $x = \frac{j}{j_D}$ , and  $y_0 = \frac{\mathcal{L}_k(x=1)}{\mathcal{L}_{k,0}}$ . The numerical fit to this formula is provided for different temperatures, and for  $T = 0.5T_c$  (which is close to the temperature at which the measurements we will present in section were obtained) the dependence of both  $\mathcal{L}_k$  and  $\lambda$  on the current are shown in figure 2.6.

While this effect has not been included in our model, it is likely to lead to a less-peaked current distribution at the edges, and thus the values of penetration depth obtained in this work might be overestimated, as  $\lambda$  steeply rises by almost 20% approaching the depairing current. Nevertheless, by considering that the switching current of a nanowire not in the *Likharev's limit* is always lower than the depairing current (see section 1.5), the effect is more limited. If the value  $j_D = 1.67j_{SW}$  reported by Berggren et al. [42] is used, the relative change in  $\lambda$  is no more than 3%.



## Chapter 3

# Design and fabrication process

This chapter addresses the fabrication process, starting from the deposition of thin niobium nitride films (section 3.1) and their characterization in terms of thickness, critical temperature and sheet resistance; we discuss the microbridges layout in section 3.2 and their fabrication in section 3.3.

### 3.1 Thin film deposition and characterization

The superconducting material employed in this work was niobium nitride (NbN). Several methods have been demonstrated for the deposition of NbN thin films, including atomic layer deposition [43], chemical vapor deposition [44], and reactive magnetron sputtering [45]. The properties of the films (e.g. superconducting critical temperature and resistivity) that can be obtained with any of these methods vary substantially depending on stoichiometry, substrate, and several other parameters.

The QNN Group developed a DC reactive magnetron sputtering with an applied RF bias process, optimized for detectors. In this work we applied the same technique, reported in detail in the supplementary material of [46].

We made use of either Si substrates with 300 nm thermal SiO<sub>2</sub> or Al<sub>2</sub>O<sub>3</sub> (sapphire) ones, previously covered in photoresist, which were diced in 1 × 1 cm<sup>2</sup> pieces, then cleaned with sonication in acetone and IPA for 5 minutes, followed by a 100W oxygen plasma ashing for 3 minutes. The films were deposited in an AJA Orion sputtering system, equipped with a 99.95% pure niobium target, in a plasma of argon in DC current controlled mode at 400 mA, with a flow of nitrogen gas and an applied 50 W RF bias.

Three properties are of interest for the deposited films: sheet resistance, thickness and the superconducting transition temperature  $T_c$ .

### Sheet resistance

Sheet resistance was measured by means of an Everbeing SR-H62 four-point probe with a spacing of 62.5 mils ( $\sim 1.6$  mm) connected to a Keithley 2400 source meter in 4-wire operation mode. Current is sent through the outer pins of the probe and the voltage is sensed across the inner ones. The pins were aligned to the center of the chip and the measurement was repeated along two directions and averaged.

In order to obtain the value of sheet resistance from the resistance measured by the source meter, the formula

$$R_{\square} = \frac{\pi}{\ln 2} KR \quad (3.1)$$

can be employed, valid for non-conductive substrates, where  $K$  is a numeric correction factor that accounts for the finite dimensions of the film. Its value is obtained with the analytical formula

$$K = \left( 1 + \frac{1}{\ln 2} \cdot \ln \left[ \frac{1 + 3 \left( \frac{s}{d} \right)^2}{1 - 3 \left( \frac{s}{d} \right)^2} \right] \right)^{-1} \quad (3.2)$$

for squared samples with a width  $d$  and a spacing  $s$  between the probes, or by means of finite element models. Using  $d = 10$  mm and  $s = 1.5875$  mm, a correction factor of 0.818 is obtained with the analytical formula and 0.8443 with FEM.

### Critical temperature

The superconducting transition temperature, or critical temperature  $T_c$ , is obtained by 4-point resistance measurements at cryogenic temperatures.

We employed a custom-made cryostat equipped with a temperature sensor, a heater and a 6-channel multiplexed 4-point probe system. The temperature of the cryostat is lowered until it reaches a baseline set by the user (the minimum is 3.5 K), then ramped up to 25 K, while the resistance values are read out and logged at a frequency of approximately 5 Hz. The value of  $T_c$  is defined as the one at which the resistance is half the one measured at 20 K.

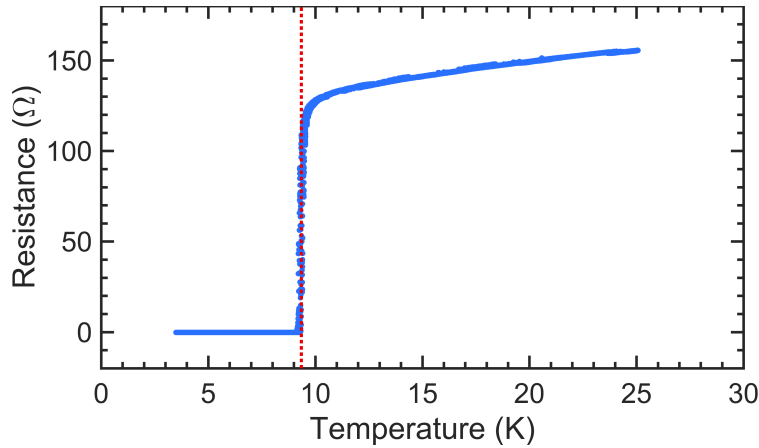


FIGURE 3.1: Results of the four-point resistance measurements performed between 3.5 and 25 K for the sample SPF556. The superconducting transition temperature  $T_c$ , defined as the temperature for which  $R(T = 20\text{ K}) = 2R(T_c)$ , is at 9.4 K, and is indicated by the red vertical line in the graph.

A measurement is reported in figure 3.1 as an example, showing the value of  $T_c$  and the behaviour of the resistance in the range 3.5–25 K.

### Thickness

Several techniques are available to measure the thickness of the sputtered films, and some of them can only be used on certain substrates. At first approximation, the film thickness is proportional to the deposition time, and by exploiting a database shared with other users of the sputtering tool, an approximate value of the thickness based on the deposition time can be obtained. The sheet resistance is also inversely proportional to the thickness, if the resistivity is assumed constant.

A more quantitative method is the use of ellipsometry, with a model developed by O. Medeiros, part of the QNN group, on a FilmSense FS-1 ellipsometer. The model works accurately on silicon substrates with a thermal oxide on top, but fails for sapphire substrates; moreover, the instrument provides accurate results for absorbing films, such as NbN, only up to 40 nm. Another technique, related to ellipsometry, that can be employed is X-ray reflectivity (XRR).

Finally, for sapphire substrates, a measurement of the thickness is possible by profilometry or atomic force microscopy (AFM) on patterned structures, after resist stripping. This is because the  $\text{Al}_2\text{O}_3$  substrate acts as an etch stop. In the case of silicon substrates the technique can not be used as silicon oxide (both grown or native)

Sample name	Dep. time [s]	$R_{\square}$ [ $\Omega$ ]	$T_c$ [K]	$t_{\text{ellips.}}$ [nm]	$t_{\text{XRR}}$ [nm]	$t_{\text{profil.}}$ [nm]
SPF224	424	102	9.7		20.3	23
SPF555	380	136	9.2	17.6	17.3	
SPF556	550	92	9.4	26.7	29.2	
SPF558	800	63	9.2	46.2	40.2	
SPF709	600		9.1		31.2	34

TABLE 3.1: Deposition time, sheet resistance and thickness measured with different methods for the films used in this work.

is partly etched in the reactive ion etching process.

Table 3.1 reports the properties of all the films deposited in the scope of this work.

## 3.2 Chip layout design

The layout of the devices was created with the aid of two tools: LayoutEditor, a visual editor for GDSII, and the phidl Python library [47], based on gdspy and optimised for the design of SNSPDs. While our work does not include detectors, we exploited the library to obtain in a straightforward way microbridges and nanowires layouts.

Microbridges, as shown in section 3.3.2, are fabricated using a negative-tone e-beam resist; only the outline of the device is thus written, effectively separating the bridge from the surrounding film. In order to fabricate wires that range from 100 nm to 100  $\mu\text{m}$  in width, several designs were explored over the course of this project. We will depict the optimal one, both for wires above 2  $\mu\text{m}$  in width (which we arbitrarily call microbridges) and below (nanowires). The distinction is due to the fact that, while for nanowires the current can be considered uniformly distributed, this does not hold true for wires approaching the Pearl length. Moreover, the large dimensions force different layout choices to maximize the number of devices on a single chip.

Microbridges (of which an example is shown in figure 3.2):

- range in width from 2 to 105  $\mu\text{m}$ ;
- have all the same aspect ratio, with the length usually being 2.5 times the width;
- have an outline of 5  $\mu\text{m}$

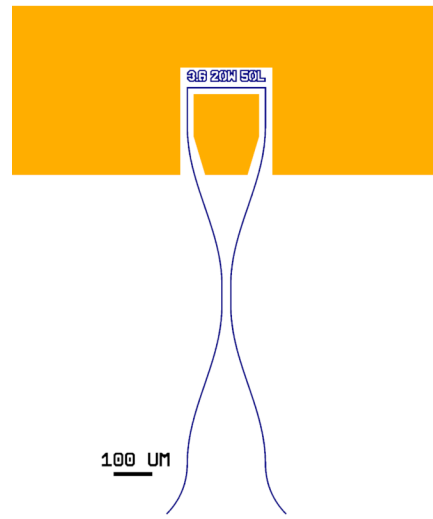


FIGURE 3.2: Design schematics of a microbridge. Gold pads are in orange; outline of the wire, written with e-beam lithography, is in blue

- are open on one side, as the ground is placed on the side of the signal pad;
- are 200  $\mu\text{m}$  wide on the closed side where the current is applied;
- the connection between the larger part and the smallest is made with a sinusoidal curve;
- they do not present any edge on the return path for the current, and the outline is expanded towards the outside as to avoid premature switches (see below);
- have two pads, a central one for the signal and an outer one, which extends above and on the sides of the device, for the ground.

Nanowires (figure 3.3) are designed in a similar way, but due to different current distributions and space restrictions:

- the connection between the smaller part (50–2000 nm) and the contact (200  $\mu\text{m}$ ) is made in two steps, with an intermediate connection 10  $\mu\text{m}$  wide. The largest parts are connected with straight lines, while the smallest are routed to the intermediate ones with optimal curves shown by Clem and Berggren [48] to reduce current-crowding;
- the outline for the smallest part is 150 nm, while the pad outline is kept at 5  $\mu\text{m}$  as for the larger devices.

If a path patterned on a thin film has a turn or contains a sharp edge, current

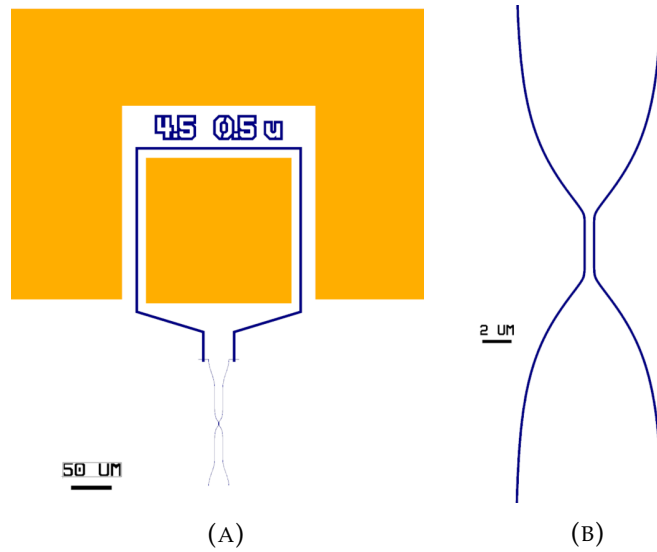


FIGURE 3.3: Design schematics of a nanowire (a). Gold pads are in orange, device is in blue. (b) shows a detail of the active area of the device

flowing in it mostly concentrates on the inner part of the curvature. This effect, typical for normal metals, also applies to superconductors, where the local increase of the current density results in an overall reduction of the critical current for the pattern. This phenomenon is called *current crowding*. Clem and Berggren [48] showed optimally rounded curves for bends, turnarounds and connections that minimize current crowding in the case of uniform current distribution in thin films, which corresponds to the limits  $t \ll \lambda$  and  $w < \Lambda$ . In the case of microbridges,  $w > \Lambda$ , and thus the curves can not be used to minimize current crowding in this case.

Nevertheless, the phenomenon exists even for non-uniform current distributions and was experimentally observed in the course of this work. An initial version of the layout included a very sharp edge at the end of the wire. When the critical current was measured, variations of up to 25% in the value could be found between different devices of the same width which showed no fabrication issues on both optical and scanning electron micrographs. The variance might be caused by the presence of an infinitely – on the layout – sharp edge, at which the current density diverges according to London equations, that in some cases causes a premature switch for the wire.

With the improved layout we previously described, we were able to reduce the variance in the critical currents of identical bridges down to 5 % or less, and when

wires with reduced switching current were observed, it was possible to link the cause to defects on the film or fabrication issues. We thus expect to have overcome current crowding issues in our devices.

### 3.3 Fabrication process

In this section we present the process for patterning microbridges on niobium nitride films, which involves two lithographic steps. The first one, described in section 3.3.1, allows the patterning of gold contact pads with direct write photolithography; the second one, shown in section 3.3.2 employs electron-beam lithography to write the microbridges structures. Finally, we discuss the details of an improved fabrication process for nanowires in section 3.3.3.

#### 3.3.1 Electrical contact pads

Gold pads are patterned on the niobium nitride film in order to allow a good electrical contact between the film and the probes of the cryogenic probe station used in the measurements (see section 4.2).

After the deposition, niobium nitride films are usually covered in photoresist to prevent any further oxidation of the film. It was thus necessary, prior to starting the fabrication process, to remove the photoresist with sonication in solvents (acetone, methanol and isopropyl alcohol), followed by drying with  $N_2$ . A bi-layer lift-off process was then employed, composed of the following steps, as depicted in figure 3.4:

- polymethylglutarimide – PMGI SF9 was spun at 4500 rpm for 1 min, then baked for 90 seconds at 180 °C;
- positive-tone photoresist Microposit S1813 was spun at 4500 rpm for 1 min, then baked for 90 seconds at 100 °C;
- the sample was exposed by means of direct writing photolithography on Heidelberg  $\mu$ PG 101, using 7 mW power and 20% laser duty cycle;
- the chip was developed with the TMAH-based developer Microposit MF CD-26 for 60 s, then rinsed in deionised water and dried with  $N_2$ ;
- a stack of 5 nm Ti (which acts as an adhesion layer for gold) and 50 nm Au layer were deposited with an electron beam evaporation system;

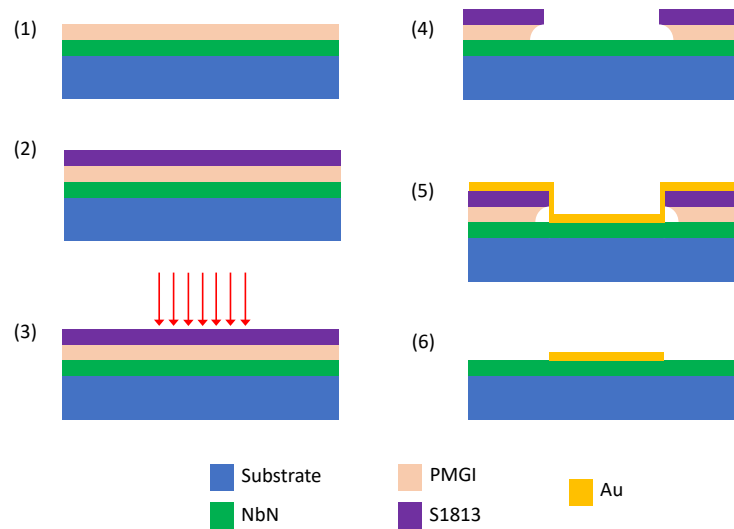


FIGURE 3.4: Schematics of the process flow for the fabrication of gold pads via bilayer liftoff: (1) after substrate cleaning, PMGI is spin-coated at 4500 rpm for 60 s and baked at 180 °C for 90 s; (2) S1813 is spin-coated at 4500 rpm for 60 s and baked at 100 °C for 90 s; (3) photoresist is exposed by direct write lithography with Heidelberg  $\mu$ PG 101, laser power 7 mW, duty cycle 20%; (4) the sample is developed in CD-26 for 60 s, then rinsed in deionized water and dried; (5) gold is deposited with e-beam evaporation; (6) lift-off is performed by sonication in acetone for 3 minutes and, after IPA rinse and dry, by dipping in CD-26 for 45 s, followed by deionized water rinse and dry.

- lift-off of the metal layer was performed by sonication in acetone for 3 minutes, the sample was then rinsed with IPA and dried; the remaining PMGI was removed in CD-26 for 45 s, followed by deionized water rinsing and N<sub>2</sub> drying.

Brief descriptions of the direct write technique and the bi-layer liftoff process are provided below.

### Direct Write Lithography

Direct write lithography is an optical lithography technique where the radiation source to expose the desired pattern on the photoresist is not transmitted through a mask, but comes from a tightly focused laser beam that is scanned over the area to be exposed. DWL has two main advantages: it is a maskless lithography technique, which reduces the costs for the fabrication of devices on a small scale, and allows changes of design, particularly useful in a research environment where adjustments to the process are continuously necessary.

The NanoStructures Laboratory is equipped with a Heidelberg  $\mu$ PG 101, a compact tabletop pattern generator with a diode laser at 405 nm, which allows the use of traditional photoresists. While usually employed for the writing of photomasks, it can be used for direct write lithography (DWL). The tool is not designed for very small chips as the ones employed in this work ( $1 \times 1 \text{ cm}^2$ ), and it has to be carefully operated in fully manual mode, together with the use of a vacuum mask on the sample holder in order to concentrate the vacuum on the central hole, onto which the sample is placed.

### **Bi-layer lift-off process**

The bi-layer lift-off used in this work is based on the presence of a sacrificial layer of PMGI SF9 below the photoactive compound, in this case S1813. The process has two main advantages over single layer traditional lift-off: it allows very high resolution features (sub  $0.25 \mu\text{m}$ ) [49] and improves feature edge shape, reducing the presence of excess material (*fencing walls*) [50].

S1813 can be developed using a TMAH-based developer, which is also a remover for PMGI, thus effectively allowing for single-step development. Moreover, PMGI is photoreactive at deep-UV wavelengths, from 240nm to 290nm [49], but it's completely transparent at the photolithography wavelength we employed (405 nm).

During development the exposed S1813 gets dissolved, together with the PMGI underneath, which creates an undercut of a few hundreds of nanometers, clearly visible with an optical microscope; its presence effectively allows a more controlled and accurate lift-off.

The lift-off process of the evaporated gold-titanium layer can be done slowly, leaving the sample in Microposit 1165 remover – a mixture of organic solvents whose main component is N-Methyl-2-pyrrolidone (NMP) – overnight, removing both resist layers at the same time, or with a quicker process which involves sonication in acetone for 3 minutes and a 45 seconds rinse in CD-26 [51]. This last process was chosen, as it helps avoid gold redeposition, thanks to the presence of the PMGI layer which is not entirely removed in acetone.

### 3.3.2 Microbridges patterning

Microbridges/nanowires - which range in width from 100 nm to more than 100 micron, were fabricated with Electron Beam Lithography (EBL). The choice of EBL instead of optical lithography is dictated by the need of a precise control of the dimensions and, in particular, of the edge roughness.

The Heidelberg direct writing tool illustrated in section 3.3.1 allows a minimum feature size of 1 $\mu$ m and edge roughness of 120 nm, making it unsuitable for the patterning of the smallest bridges.

#### Electron beam lithography

Electron beam lithography is a maskless lithography technique that employs a focused electron beam at high acceleration voltages (in the range 10–100 kV) to imprint a pattern on a special resist which is sensitive to electrons. In the work here reported, we used an Elionix ELS-F125 system equipped with a 125 kV column, providing a beam diameter of 1.7 nm at low writing current, and effectively allowing line dimensions down to 5 nm. Differently from the Heidelberg tool, this piece of equipment operates in a vector scan mode, thus making the total writing time directly proportional to the exposed area.

The tool is provided with a software which allows to load any GDSII design and to convert it in a format readable by the machine. The total area to write is divided into multiple *fields* by the software, each with an area up to 500  $\times$  500  $\mu$ m<sup>2</sup>; during the exposure of a single field the mechanical stage where the chip is placed does not move, and the beam is deflected with a set of lenses to expose the desired pixels. No aberration is present on the edges of a field due to a dynamic correction of the electron beam focus and stigmatism operated automatically by the tool.

If a feature is larger than the afore-mentioned area, it will be split into multiple fields, which may result in stitching errors due to the precision of the mechanical movement of the stage. The magnitude of these errors is – according to Elionix – in the order of 30 nanometers, but sharp edges due to misalignment can be mitigated by using a multi-pass procedure that doubles the number of fields and overlaps

them, writing them with half the desired dose each. This way the misalignment remains, but there will be no sharp edge thanks to the multiple writings on the same area. Most of the microbridges we wrote are longer than 500  $\mu\text{m}$  in total, and therefore split into multiple fields, which is the reason why we opted for a multi-pass write.

We employed a positive-tone e-beam resist, ZEP520A, developed by Zeon Nippon. When a cold development process is used with this resist, it is possible to obtain sub-35 nm wide lines [52] with edge roughness of approximately 3 nm [53]. ZEP520A, undiluted, was spun on the chip at 5000 rpm for 60 seconds, then baked at 180 °C for 2 minutes. The exposure was performed with an e-beam dot size of 10 nm, and a dose of 500  $\mu\text{C cm}^{-2}$ .

The alignment to the first layer was performed manually, with an iterative process which makes use of the Elionix electron beam as an SEM tool. The manual procedure can produce alignments to less than 20 nm, but due to the large dimensions and roughness of the marks – obtained with optical lithography – we chose to end the process as soon as the alignment precision as reported by the software was below 100 nm.

As previously mentioned, the use of a cold development process has been shown to allow for sub-35 nm features patterning and for improved edge roughness [52]. While the features of most of the microbridges fabricated in this work are sensibly bigger than such dimensions, our interest in such process comes from the lower edge roughness that can be achieved. We thus developed the exposed pattern in o-xylene at 0 °C for 90 seconds, followed by a rinse in isopropyl alcohol at room temperature for 30 seconds.

### **Etching**

In order to transfer the pattern from the resist onto the niobium nitride film, and to obtain an anisotropic profile, we employed a dry etching technique. The samples were etched with a PlasmaTherm reactive ion etching (RIE) tool with  $\text{CF}_4$  as reactive gas and helium as carrier, with a plasma power of 50 W. This process has been shown to provide good results for the fabrication of niobium nitride detectors [54].

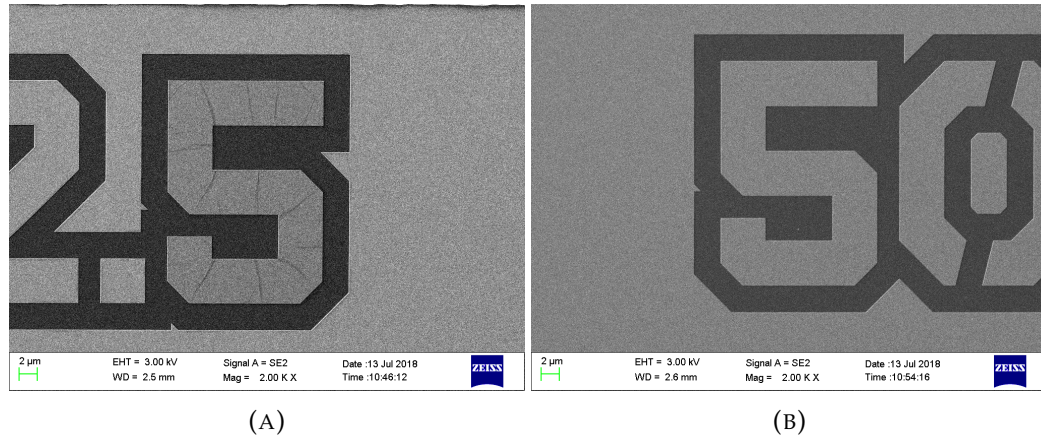


FIGURE 3.5: SEM micrographs after resist stripping for two different etching processes: RIE  $\text{CF}_4$  50W for 6 minutes (a) or  $3 \times 2$  minutes (b). The use of shorter etch times allows the complete removal of the electron-beam resist while longer etches result in resist burning.

Work made by O. Medeiros in the QNN group showed that the etch rate for bare niobium nitride films is in the order of  $6 \text{ nm min}^{-1}$ . Nevertheless, the effective etch rate for patterned structures is lower, due to the reduced availability of reagents at the bottom of trenches, and is influenced by the aspect ratio of the structures to be etched (larger structures are etched faster). For this reason, given an arbitrary thickness of niobium nitride films and resist, finding the correct etch time is not straightforward.

In all our chips, we included an etch square – basically a  $1 \text{ mm} \times 1 \text{ mm}$  outline patterned with EBL – that could be probed with a two-point probe to check its resistance: if it read zero, the etch was complete. This process is not without error – if the square is not connected because of fabrication defects, it becomes unusable. With this method, it was possible to obtain the optimal etch time for 20 nm films, which is of 6 minutes.

If the resist is exposed to the plasma for a long period, it can burn and become virtually impossible to be stripped after the etching process. In order to avoid it, we split the process into three separate etches, each lasting two minutes, after which the vacuum in the chamber was recovered. Figure 3.5 shows SEM micrographs obtained after stripping the resist, for a long etch and multiple short etches. In the first case, noticeable ZEP residues were present on the film, while in the latter, no visible traces remained.

One last concern comes from the resistance of the electron beam resist to the etch

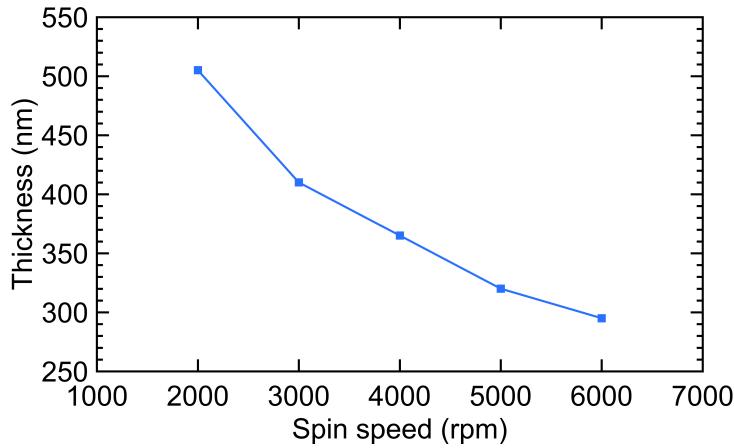


FIGURE 3.6: Spin curve for ZEP520A, from [55].

Initial thickness (nm)	Final thickness (nm)	Etch time (min)	Etch rate (nm/min)
315.8	293.2	2	11.3
324.4	280.7	2 × 2	10.9

TABLE 3.2: Etch rate for ZEP520A spin-coated at 5000 rpm on silicon and etched with RIE  $\text{CF}_4$  at 50W.

process. The expected thickness of ZEP520A, spin-coated as previously described, is around 310 nm (see figure 3.6. The effective thickness of the film can be obtained by means of ellipsometry, using the parameters of Cauchy's equation

$$n = A + \frac{B}{\lambda^2} + \frac{C}{\lambda^4} + \dots \quad (3.3)$$

$A = 1.541093$ ,  $B = 4.113002 \times 10^5$ ,  $C = 4.070357 \times 10^{12}$  as provided by the manufacturer [55], with the wavelength  $\lambda$  measured in Å.

Two bare silicon chips were spin-coated with ZEP520A and their thickness measured with ellipsometry, and found to be comparable with the expected one. The thickness was measured again after one and two 2-minutes RIE  $\text{CF}_4$  etches, respectively. The etch rate was found to be slightly above 10 nm/min in both cases, as shown in table 3.2.

### Process recipe

For the reader's convenience, we report concisely the fabrication steps for the microbridges patterning, which are schematically depicted in figure 3.7. Figure 3.8 also shows an optical and SEM micrograph of complete devices.

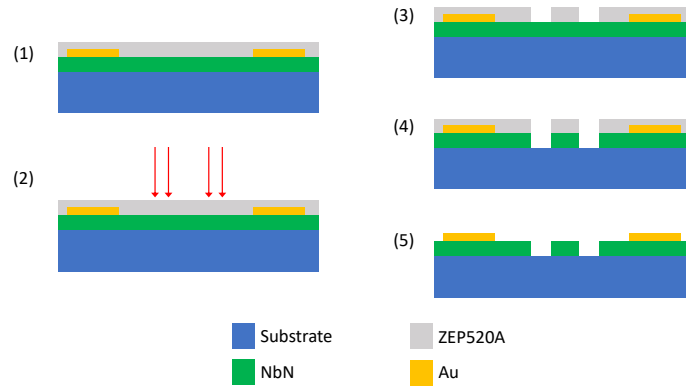


FIGURE 3.7: Schematics of the process flow for the fabrication of wires: (1) ZEP520A is spin-coated at 5000 rpm for 60 s on the chip with previously patterned gold contact pads, then baked at 180 °C for 2 minutes; (2) e-beam exposure is performed with an Elionix 125 KeV tool at a dose of  $500 \mu\text{C cm}^{-2}$ ; (3) the sample is developed in o-xylene at 0 °C for 90 s, rinsed in IPA for 30 s, then dried; (4) the wires are etched via RIE  $\text{CF}_4$  at 50 W; (5) the resist is stripped in heated NMP at 70 °C, left cooling overnight.

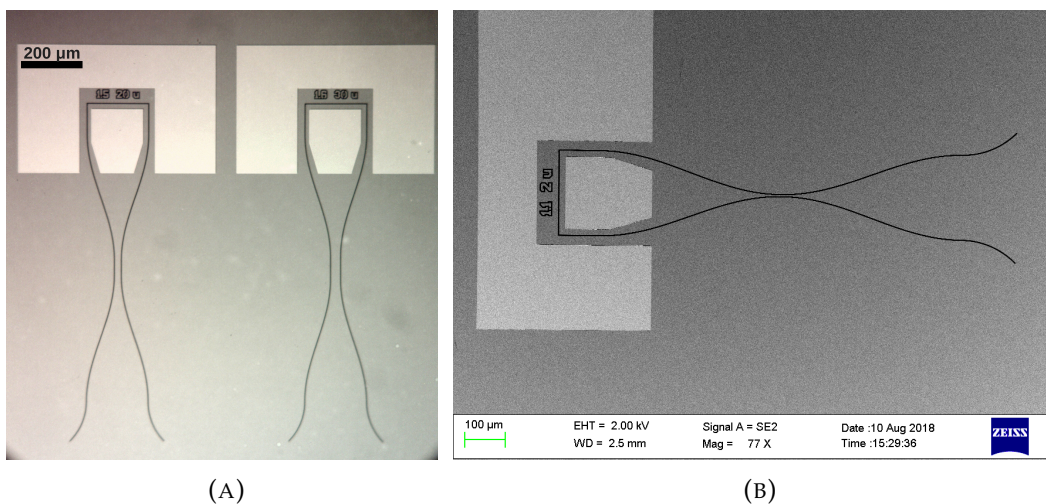


FIGURE 3.8: Final device, optical image (A) and SEM (B).

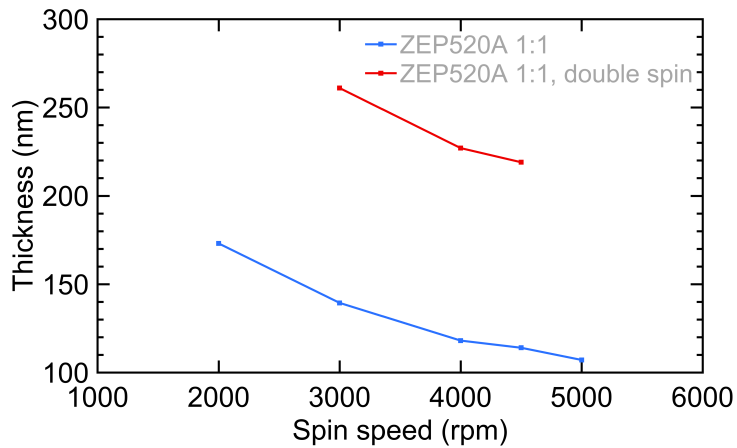


FIGURE 3.9: Spin curves for ZEP520A diluted 1:1 by volume in anisole, with 2 min bake at 180 °C (blue) and for the same resist spin coated and baked twice (red). The double spin process allows to reach a thickness that is almost double the one of the single layer.

- Electron-beam resist ZEP 520A was spun at 5000 rpm for 1 min, then baked for 2 minutes at 180 °C;
- the pattern was imprinted with a 125 keV EBL tool, with a dot size of 10 nm and a dose of 500  $\mu\text{C cm}^{-2}$ ;
- the sample was developed in o-xylene at 0 °C for 90 s, then rinsed in isopropyl alcohol for 30 s;
- reactive ion etch with  $\text{CF}_4$  at a plasma power of 50 W was performed in 3 steps of 2 minutes each (for the 20 nm film) or until fully etched;
- the remaining resist was stripped in NMP heated at 70 °C for an hour, left overnight and sonicated for 1 minute.

### 3.3.3 Process enhancement

To fabricate wires with smaller critical dimensions, we optimized the process for a different developer, hexyl acetate, known to provide better contrast than o-xylene in the cold development process [56].

We also chose to reduce the resist's thickness, to improve the aspect ratio for small (sub-100 nm) features. As shown in the ZEP520A spin curves reported by the manufacturer and in figure 3.6, it is not possible to obtain resist thicknesses below 300 nm without using a diluted resist. We employed a 1:1 solution of ZEP520A in anisole, and obtained the spin curves after the standard bake at 180 °C, measuring

the film thickness by means of ellipsometry. The results are shown in figure 3.9, which also displays the thickness obtained with a double spin and bake process that can be applied to obtain intermediate thickness values. The chosen process was a double spin coating and baking of ZEP520A 1:1 solution at 4000 rpm, leading to a thickness of approx. 220 nm.

We employed a cold development process at 0 °C for 60 seconds, followed by an IPA rinse and N<sub>2</sub> drying. In order to obtain the correct e-beam dose for the process, a dose matrix – i.e. a repeated pattern with features and critical dimensions similar to the desired final ones, exposed at different doses on the same chip – was patterned with EBL, and the post-development effective dimensions were measured with SEM. Doses ranging from 350 to 850  $\mu\text{C cm}^{-2}$  were used. Figure 3.10 shows the results for three different doses: 500, 550 and 600  $\mu\text{C cm}^{-2}$ . Design dimensions were 150 nm lines with 150 nm pitch. The lowest dose shows under-developed regions, the highest is over-developed and resulted in lines of 160 nm, while the 550  $\mu\text{C cm}^{-2}$  resulted in a precise reproduction of the designed layout. The optimized dose for the exposure of 220 nm-thick ZEP520A, developed in hexyl acetate at 0 °C for 60 seconds, is thus 550  $\mu\text{C cm}^{-2}$ .

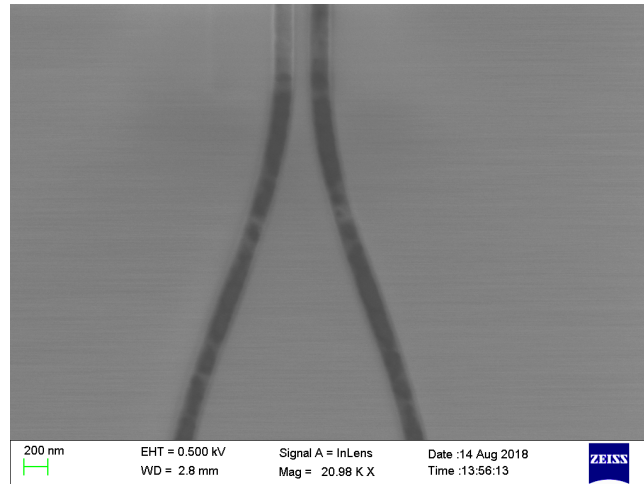
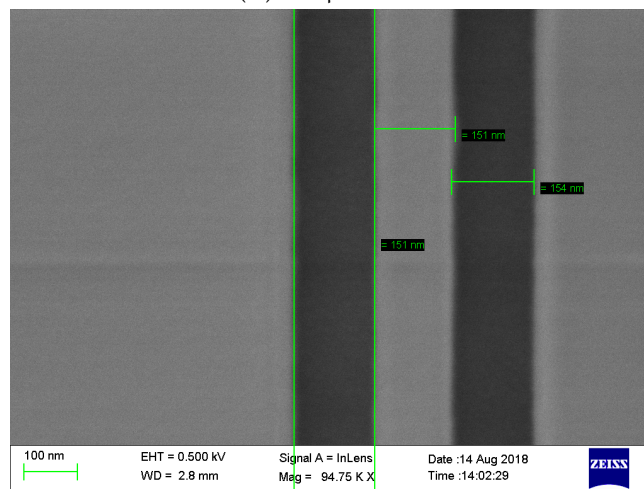
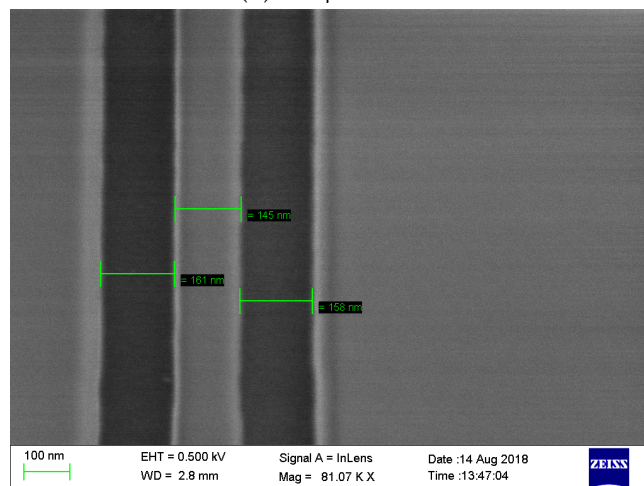
(A)  $500 \mu\text{C cm}^{-2}$ (B)  $550 \mu\text{C cm}^{-2}$ (C)  $600 \mu\text{C cm}^{-2}$ 

FIGURE 3.10: Post-development feature dimension measurements with SEM, for three different doses, 500 (a), 550 (b) and 600  $\mu\text{C cm}^{-2}$  (c). Dark areas represent exposed and developed parts, grey areas are covered in resist. The lines were designed to be 150 nm wide, with a pitch of 150 nm. The lowest dose displays under-developed regions, which can be identified by the changes in contrast along the patterned zone. The highest dose is over-developed, as the features reached dimension of around 160 nm, while the dimensions of the pattern with intermediate dose match the designed ones.



## Chapter 4

# Experimental results and discussion

We present in this chapter the results of cryogenic measurements for the critical current of the devices we described in chapter 3. In section 4.1 we introduce the measurement setup employed and the challenges it provides, in section 4.2 we present the results obtained by probe station measurements at a temperature of 4 K, while a discussion of the temperature dependence is given in 4.3.

### 4.1 Measurement setup

The measurement set-up for the experiment, remembering that we aim at finding a simple and fast method to determine  $\lambda$  of NbN films, is very straightforward, and mostly consist on a current source and a voltage meter.

Figure 4.1 shows a schematic of the final set-up we employed. It consists of a low-noise DC current source Yokogawa GS200 (with a noise level of 3 mA<sub>pp</sub> in the

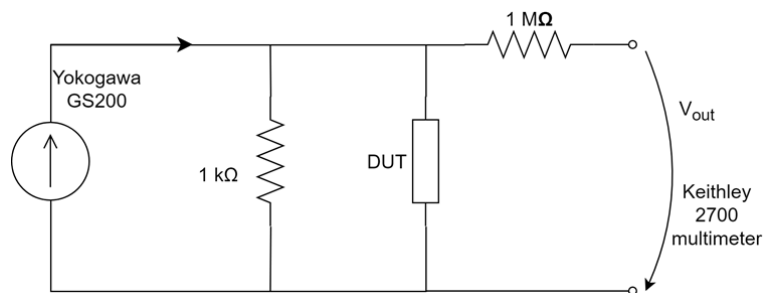


FIGURE 4.1: Setup for critical current measurements. A Yokogawa GS200 sources current which goes through the microbridge and a 1 kΩ shunt resistor. The voltage on the DUT is read by a Keithley 2700 multimeter with an input resistance of 1 MΩ.

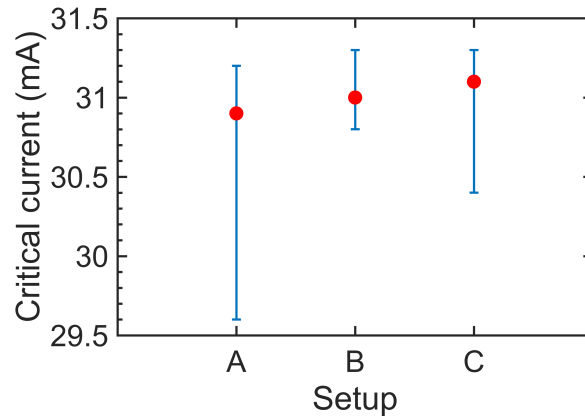


FIGURE 4.2: Comparison between different setups:

**A:** Keithley 2001 current source, Keithley 2700 with  $R_s = 1\text{ M}\Omega$

**B:** Yokogawa GS200 current source, Keithley 2700 with  $R_s = 1\text{ M}\Omega$

**C:** Yokogawa GS200 current source, Keithley 2700 without input series resistance

The red dot represents the median value of 21  $I_C$  DC measurements, while the bars represent the minimum and maximum value obtained. While the median and maximum are comparable between the three setups, the combination of GS200 and input resistance to the multimeter provides the less added noise to the circuit, reducing premature switches.

100 mA range [57]), a  $1\text{ k}\Omega$  shunt resistor in parallel to the DUT, and a Keithley 2700 multimeter used to read the voltage across the device. A  $1\text{ M}\Omega$  resistor is placed in series to the multimeter for noise reduction purposes.

Several setups were experimented in order to define the optimal one; figure 4.2 shows a comparison between two different current sources, the already mentioned Yokogawa GS200 and the Keithley 2400 source meter; it also shows the influence of the resistor at the multimeter input. The critical current of a single device ( $30\text{ }\mu\text{m}$  microbridge) was measured several times with the different setups: while the average and maximum values obtained are constant, some setups give lower minimum values, which are presumably due to premature switches induced by the instruments' noise.

In order to obtain a complete I-V curve for the device, the current was slowly ramped (steps of 50 ms) from zero to the maximum chosen value, then to its negative value and then to zero. The multimeter readout at every step was integrated over 1 power line cycle (1/60th of a second), and the input current was changed at intervals of 50 ms.

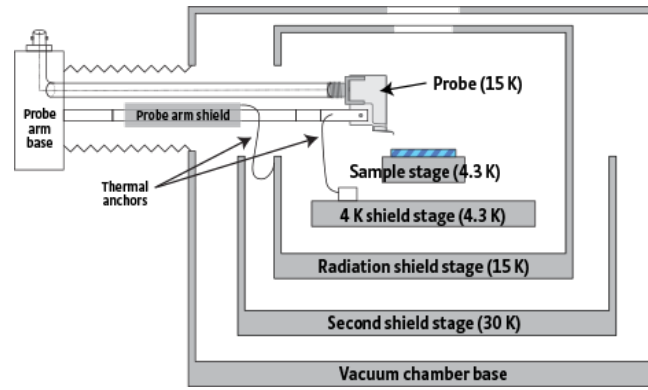


FIGURE 4.3: Cryogenic probe station schematics, from [58]

The instruments were controlled through their GPIB interfaces with a Python script using the pyVISA library, and custom-made libraries for each instrument.

## 4.2 Measurements at 4 K

### 4.2.1 Cryogenic system

Two options were available to perform measurements at cryogenic temperatures: measuring the chip by direct immersion in a dewar with liquid helium, or with a cryogenic probe station.

Liquid helium measurements require to wirebond the chip to a custom-made PCB; the signals are carried out of the dewar to the external instrumentation by coaxial SMA cables. It is a very quick and relatively inexpensive method for testing, and allows for long measurements, up to a few days. Nevertheless, the number of connectors on the PCB and cables available, as well as the crowding of wirebonds on the chip, limit the number of devices that can be measured to 12 at a time. Moreover, direct contact with liquid helium can lead to contamination.

On the other hand, the cryogenic probe station provides a turbo-pumped vacuum chamber where the chip is placed with no direct contact with liquid helium. The probe station is composed of several stages at different temperatures, as shown in figure 4.3. The sample stage is isolated from the others with a needle valve that is opened when the second shield reaches temperature lower than 77 K (temperature of nitrogen liquefaction), so that all the impurities are condensed on the outer shields and not on chip, effectively avoiding contamination. Moreover, the use of a probe

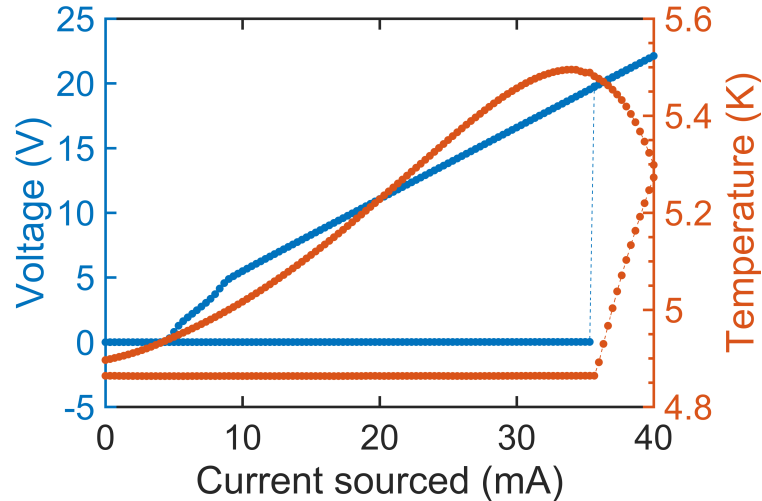


FIGURE 4.4: Temperature of the sample stage (orange), measured with a Lakeshore GaAlAs diode during the I-V measurement (blue) of a  $40\ \mu\text{m}$  bridge. The local temperature is raised by more than 1 K when the wire becomes resistive, but the cooling power of the system is sufficient to return the stage to its base temperature as soon as the wire returns in the superconducting state.

lifts any limits on the number of devices that can be tested at a time and remove the need for wirebonding. The probe spans a range of approximately  $2 \times 2\ \text{cm}^2$ , which means that up to four  $1 \times 1\ \text{cm}^2$  chips can be tested at a time. The main disadvantage of the probe station is the amount of liquid helium required to cool it down; the capacity of the recovery system owned by the QNN group effectively limits the measurements to sessions of 2-3 hours.

Overall, the probe station was the measurement method of our choice, mainly because of the possibility of measuring several devices at a time. Moreover, the probe station is equipped with temperature sensors on every stage, allowing for an accurate measurement of the temperature at which the experiment is carried out. A temperature sensor was also installed on the sample stage and connected to a Cryocon 34 temperature controller which allowed a temperature readout via GPIB. This way, we could observe the effect of heat dissipation from the bridges (see figure 4.4) and ensure that the system would return to its base temperature before a new measurement.

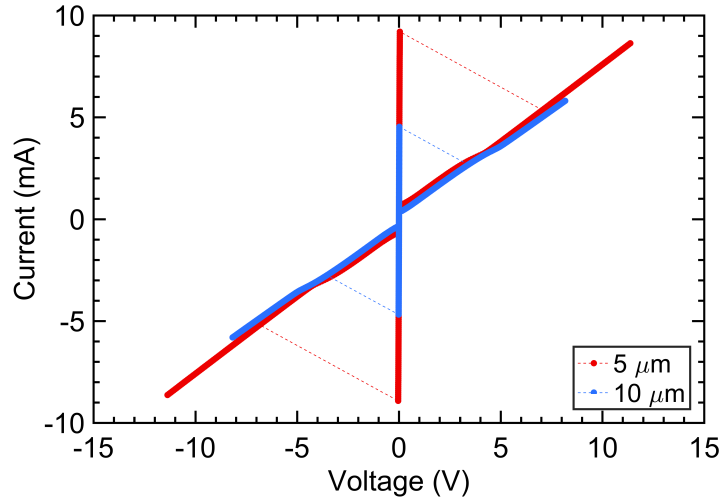


FIGURE 4.5: I-V curves from two different wires, of dimensions 5 (blue) and 10  $\mu\text{m}$  (red) respectively.

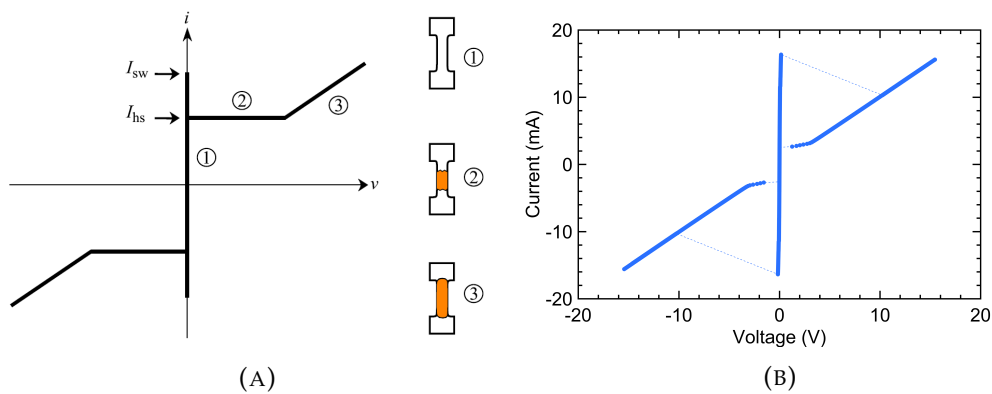


FIGURE 4.6: (A) Model of the nanowire I-V curve, reprinted from [42]. Three regimes are visible: the superconducting region (1), the normal region (3) and the hotspot plateau (2). These behaviour is clearly reproduced in the microbridges measured in our work: (B) shows the I-V curve for a 40  $\mu\text{m}$  bridge.

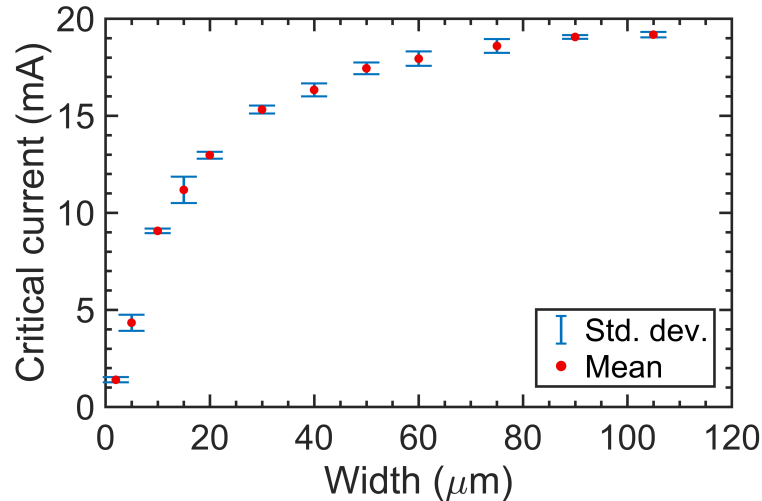


FIGURE 4.7: Critical current versus width measured from 47 devices ranging in width from 2 to 105  $\mu\text{m}$ . The error bars represent the standard deviation of data obtained from different copies of the same device.

#### 4.2.2 Results

A family of I-V curves from devices of different width, and with a film thickness of 20 nm, are shown in figure 4.5. The non-horizontal load line is due to the presence of a shunt resistor in parallel to the device under test. The hot-spot plateau [42], in which a limited region of the wire is in the normal state and the rest of it is superconducting, is particularly evident at larger widths, as shown in figure 4.6.

The results from the measurements of 47 devices ranging from 2 to 105  $\mu\text{m}$  in width and with a length of 2.5 times the width are shown in figure 4.7. Different copies of the same device show comparable values of critical current with variations lower than 5%, except for the smallest wires where the variability is mostly due to the discrete values of the measurements. Some outliers which show significantly lower  $I_c$  with respect to other devices of the same dimensions are present, and the lower values are associated with the presence of fabrication defects in the area close to the wire, as later shown by an inspection under an optical microscope.

#### 4.2.3 Data fitting

The dataset shown in figure 4.7 shows a monotonically increase of  $I_c$  as a function of width, with a saturating behaviour, which is in accordance to the hypotheses made

and the results of the FEM model of chapter 2. It is thus possible to fit the empirical data with the model in order to extract  $\Lambda$ .

As explained in section 2.2 though, the London equation which lead to the current distribution is solved by choosing arbitrarily the value of the edge current. Therefore, in order to compare the model with the data, it is necessary to know the value of  $J_c$ .

Some options can then be followed:

- Assume a uniform current distribution for the narrowest wires ( $2\ \mu\text{m}$ ) and extract  $J_c$  by dividing the measured  $I_c$  value by the cross section of the wire. This method has two disadvantages: as shown in figure 2.2, the current distribution is non-uniform even at micrometre widths, and the value of  $I_c$  for the narrowest wires have a bigger uncertainty given by the steps at which the current is increased. Finally, smaller wires have higher probability of being affected by fabrication-related issues, such as edge roughness, effectively lowering the value of  $J_c$
- Fit the experimental data with a high-order polynomial, or better a sigmoid function such as an arctangent, and extract  $J_c$  from the slope of the curve at the origin. The main drawback here is that the choice of the type of fitting curve strongly influence the final value.

We opted for a third solution, which provides a very straightforward way of fitting the data without knowing the value of the critical current density, and allows to extract it directly from the fit parameters. We divided the empirical data with the *reduction factor* we introduced in figure 2.4 for different values of  $\Lambda$ . What is obtained is then the  $I_c$  vs width relation if the current distribution was uniform in the wire. We fitted the results with a line of the type

$$I_c = J_c t(w - w_0) \quad (4.1)$$

and chose  $\Lambda$  based on the best fit. Since multiple devices were measured for every width value, we assigned a weight to every point of the fit inversely proportional to the variance of the measured  $I_c$ . We considered two parameters to determine the optimal fit:

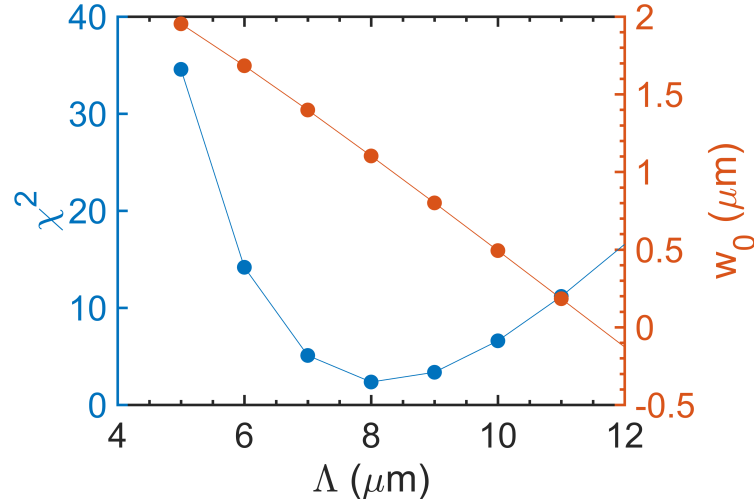


FIGURE 4.8: Values of  $\chi^2$  and the fit intercept  $w_0$  for  $\Lambda$  ranging from 5 to 12  $\mu\text{m}$ . The choice of fit could be made in order to minimize the intercept (which has no physical meaning, except for a few tens of nanometers which might be linked to an error in the dimension measurement) or to achieve the lowest value of  $\chi^2$ , which is a goodness-of-fit indicator.

1. a goodness-of-fit indicator, coming from a  $\chi$ -squared test [59, p. 268];
2. the value of the intercept  $w_0$ , which we expect to be close to zero.

In figure 4.8 we show both the value of the reduced  $\chi^2$  and  $w_0$  for a range of  $\Lambda$  values. While the  $\chi^2$  is minimum at  $\Lambda = 8 \mu\text{m}$ , the intercept goes close to zero at  $\Lambda = 11 \mu\text{m}$ ; the arbitrariness in the choice of the value of  $\Lambda$  that best fits the data becomes then evident.

By using the value of thickness of 20.3 nm obtained by XRR (see table 3.1), one gets a value of the London penetration depth between 402 and 472 nm at the measured temperature. Applying the temperature dependence of  $\lambda$  from equation 1.2 and a critical temperature of 9.7 K, the value of  $\lambda(0)$  obtained is between 389 and 457 nm. Moreover, the value of  $J_c$  extracted from the fit, as shown in figure 4.9 is between 6.2 and 8.1  $\text{MA cm}^{-2}$  which is slightly higher than the  $J_c$  measured on the narrowest 2  $\mu\text{m}$  wire (see fig. 4.11).

Values of  $\lambda$  reported for single-crystal niobium nitride are usually in the range of 180 nm [60], while for thin films deposited via DC reactive magnetron sputtering a range between 250 [61] and 370 [62, 63] nm is generally considered; some values as high as 495 nm have also been reported [64]. Such high differences can be resolved

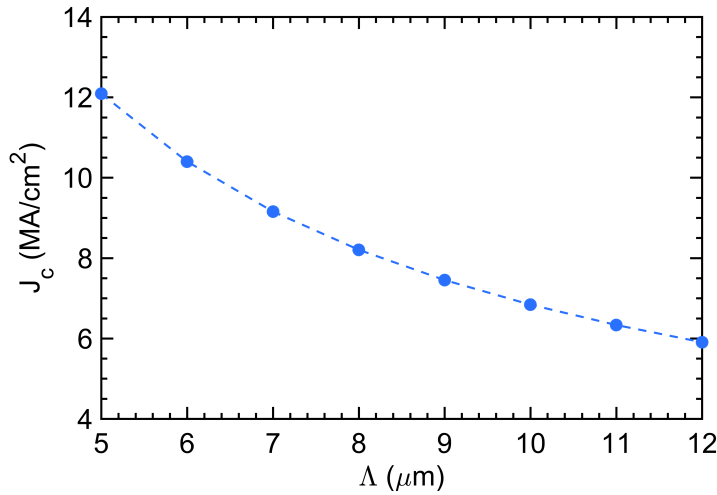


FIGURE 4.9:  $J_c$  obtained from the fit as described in section 4.2.3. The values between 6–8  $\text{MA}/\text{cm}^2$  are compatible with the measured ones on narrow wires (see figure 4.11).

by the variations in the normal state film resistivity and the superconducting transition temperature, as Hossain et al. [65] demonstrated by introducing an effective penetration depth of NbN following  $\lambda_{\text{eff}} \propto \sqrt{\frac{\rho_n}{T_C}}$ .

The values we extracted are thus compatible with what is reported in literature. The relatively high value could be linked to the room-temperature deposition process which produces films with lower critical temperature.

#### 4.2.4 Film aging

The same film from which the measurements in figure 4.7 were obtained, was measured again with the same setup after 45 days. During this time period the chip was exposed to air for several hours at a time and stored in a nitrogen purged cabinet. Moreover, the chip was subjected to two additional thermal cycles from room to cryogenic temperatures and vice versa to acquire other measurements. The dataset obtained after exposure to air and thermal cycling is shown in figure 4.10: the onset of saturation is now at much higher widths and the total current that can be sent through the wires is increased; nevertheless, the values of critical currents for narrow wires are comparable to the ones obtained previously. The change would be most probably due to modifications in the film that led to a change in the penetration depth; the change in thickness due to oxidation can also be taken into account,

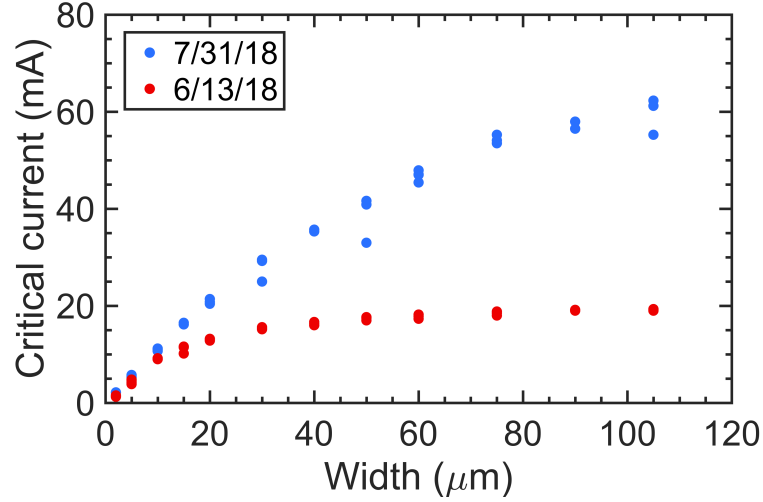


FIGURE 4.10: Combined effects of aging and thermal cycling: the first measurement (red), performed immediately after the fabrication process minimizing the exposure to air, results in lower overall current and an onset of saturation at lower widths than measurements performed after 45 days of air/N<sub>2</sub> exposure and two additional thermal cycles (blue).

but it is less likely to be the predominant effect as that would imply a variation in the measured values of  $J_c$  at low width.

### 4.3 Temperature dependence

The theoretical temperature dependence of the critical current in superconductors is provided by Bardeen's formula [23]

$$J_c(T) = J_{c0} \left[ 1 - \left( \frac{T}{T_c} \right)^2 \right]^{3/2} \quad (4.2)$$

where  $J_{c0}$  is the critical current density at zero temperature and  $T_c$  is the critical temperature.

In order to measure the temperature dependence of the bridges we fabricated, we employed a vibration-isolating cryostat [66] with free-space optical access and six coaxial SMA connections, able to reach a base temperature  $T = 2.9$  K with a Cryomech pulse-tube cryocooler. The system is equipped with a heater and a temperature sensor connected to a Cryocon 34 temperature PID controller, which allows to set the temperature of the sample stage.

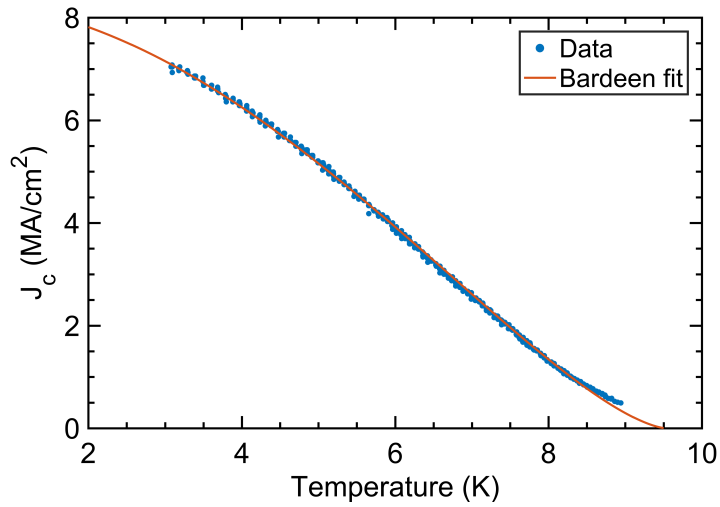


FIGURE 4.11:  $J_c$  vs temperature for a 2  $\mu\text{m}$  bridge. The data (blue) show good agreement with Bardeen's formula, for which the fit provided a value of  $J_{c0} = 8.36 \text{ MA cm}^{-2}$  and  $T_c = 9.55 \text{ K}$ .  $J_c$  was computed dividing the measured critical current by the wire cross section, thus assuming uniform current distribution.

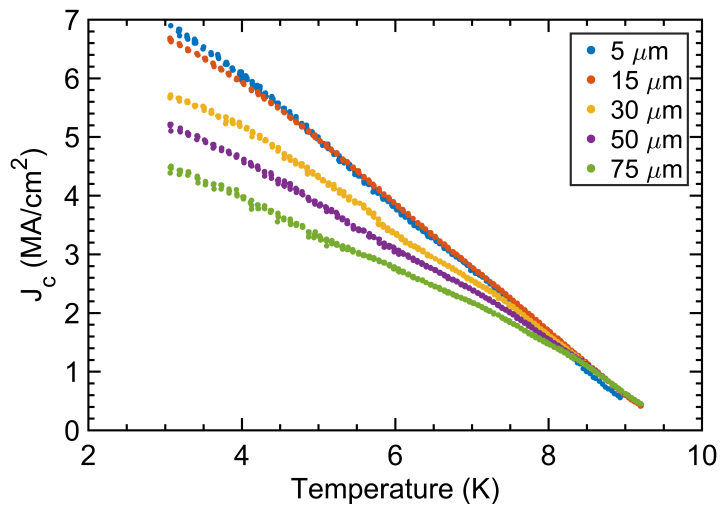


FIGURE 4.12: Critical current density ( $J_c = I_c/wt$ ) for wires of increasing widths. While the behaviour of narrow wires match over a wide range of temperature,  $J_c$  gets lower at low temperature for increasing width. All the curves overlap near the transition temperature, hinting on a uniform distribution due to the increase of  $\lambda$ .

The wires were measured from temperatures of 3 K up to their superconducting transition temperature with a Python custom code. The measurement setup was the same as described in section 4.1. For every set temperature, the current was ramped up until a voltage was generated across the device; at that point the current source output was turned off to avoid heating of the substrate (see figure 4.4) and the value of the switching current recorded. For every temperature, the critical current was measured 3 times, and the temperature was raised from 3 K up to 9 K and then ramped down again. At every temperature step, we waited for the stabilization of the system for 90 seconds, or until the temperature was within 1 % of the target value.

The narrowest wire (see figure 4.11) showed good agreement with Bardeen's formula, with a fitted value of  $T_c = 9.53$  K – slightly lower than the film's  $T_c$  of 9.7 K, while for wider wires (figure 4.12) the temperature dependence deviates from the theoretically predicted one; we attribute this fact to the non-uniform current distribution. Moreover, the value of  $J_{c0} = 8.36$  MA cm<sup>-2</sup> is compatible with what reported elsewhere [67].

Moreover, it's possible to observe a reduction in the critical current density (defined as the measured critical current divided by the cross section) for wide wires at low temperatures, while the curves overlap when approaching the transition temperature. Similar results were already reported in literature for NbN bridges [28, 29] and are another confirmation of our model: as the temperature increases,  $\lambda$  diverges (see equation 1.2) and the current becomes uniform; the critical current density thus becomes independent of the wire dimensions.

## Chapter 5

# Conclusions and future works

This work demonstrated the feasibility of a method to obtain the penetration depth of niobium nitride films. The advantage of this method is the relative simplicity in the fabrication process and the measurement setup, which is a DC I-V measurement. Moreover, if the process were to be refined, it could be possible to implement a test structure for a routine determination of the screening length on fabricated chips.

We obtained a value of  $\lambda(0)$  between 389 and 457 nm for a 20 nm film sputtered via reactive DC magnetron sputtering at room temperature, with a critical temperature  $T_c$  of 9.7 K. The values are compatible with what reported in literature, but further work is needed to refine and confirm the validity of this model.

Firstly, an independent technique for the penetration depth evaluation has to be employed as a confirmation for the extracted values. Moreover, measurements varying the film thickness or the deposition technique (and thus the transition temperature) are to be performed in order to validate the model, and to identify the correct fitting technique.

The assumption we made in our model of  $J_c$  being a property of the material and independent of geometrical properties can be verified, either by exploring the critical currents of sub- $\mu\text{m}$  nanowires carrying a uniform current, for which a fabrication process has been devised within this work, or by investigating the effect of the wire length.

Finally, the model can be improved by taking into account the dependence of the kinetic inductivity on the current density, leading to a more accurate evaluation of  $\lambda$ .



# Bibliography

- <sup>1</sup>D. van Delft and P. Kes, "The discovery of superconductivity", *Physics Today* **63**, 38–43 (2010).
- <sup>2</sup>W. Meissner and R. Ochsenfeld, "Ein neuer Effekt bei Eintritt der Supraleitfähigkeit", *Die Naturwissenschaften* **21**, 787–788 (1933).
- <sup>3</sup>F. London and H. London, "The Electromagnetic Equations of the Supraconductor", *Proceedings of the Royal Society A: Mathematical, Physical and Engineering Sciences* **149**, 71–88 (1935).
- <sup>4</sup>M. Tinkham, *Introduction to superconductivity*, 2nd ed, International series in pure and applied physics (McGraw Hill, New York, 1996).
- <sup>5</sup>J. F. Annett, *Superconductivity, superfluids, and condensates*, Oxford master series in condensed matter physics (Oxford University Press, Oxford ; New York, 2004).
- <sup>6</sup>J. Pearl, "Current distribution in superconducting films carrying quantized fluxoids", *Applied Physics Letters* **5**, 65–66 (1964).
- <sup>7</sup>N. W. Ashcroft and N. D. Mermin, *Solid state physics* (Holt, Rinehart and Winston, New York, 1976).
- <sup>8</sup>A. J. Annunziata, D. F. Santavicca, L. Frunzio, G. Catelani, M. J. Rooks, A. Frydman, and D. E. Prober, "Tunable superconducting nanoinductors", *Nanotechnology* **21**, 445202 (2010).
- <sup>9</sup>S. D. Brorson, R. Buhleier, J. O. White, I. E. Trofimov, H.-U. Habermeier, and J. Kuhl, "Kinetic inductance and penetration depth of thin superconducting films measured by THz-pulse spectroscopy", *Physical Review B* **49**, 6185–6187 (1994).
- <sup>10</sup>A. Murphy, D. V. Averin, and A. Bezryadin, "Nanoscale superconducting memory based on the kinetic inductance of asymmetric nanowire loops", *New Journal of Physics* **19**, 063015 (2017).
- <sup>11</sup>S. Doyle, P. Mauskopf, J. Naylon, A. Porch, and C. Duncombe, "Lumped Element Kinetic Inductance Detectors", *Journal of Low Temperature Physics* **151**, 530–536 (2008).
- <sup>12</sup>A. J. Kerman, E. A. Dauler, J. K. W. Yang, K. M. Rosfjord, V. Anant, K. K. Berggren, G. N. Gol'tsman, and B. M. Voronov, "Constriction-limited detection efficiency of superconducting nanowire single-photon detectors", *Applied Physics Letters* **90**, 101110 (2007).

- <sup>13</sup>C. Stevens and D. Edwards, "High temperature superconducting MM-wave photomixers", in International Topical Meeting on Microwave Photonics MWP 2000 (2000), pp. 237–240.
- <sup>14</sup>C. J. Stevens, G. Bianchi, and J. F. Ryan, "Ultrafast sampling measurements using the photomodulated kinetic inductance in high-T<sub>c</sub> superconductors", *Applied Physics Letters* **82**, 4014–4016 (2003).
- <sup>15</sup>B. Ho Eom, P. K. Day, H. G. LeDuc, and J. Zmuidzinas, "A wideband, low-noise superconducting amplifier with high dynamic range", *Nature Physics* **8**, 623–627 (2012).
- <sup>16</sup>J. Luomahaara, V. Vesterinen, L. Grönberg, and J. Hassel, "Kinetic inductance magnetometer", *Nature Communications* **5**, 4872 (2014).
- <sup>17</sup>P. K. Day, H. G. LeDuc, B. A. Mazin, A. Vayonakis, and J. Zmuidzinas, "A broadband superconducting detector suitable for use in large arrays", *Nature* **425**, 817–821 (2003).
- <sup>18</sup>S. Doerner, A. Kuzmin, K. Graf, S. Wuensch, I. Charaev, and M. Siegel, "Compact microwave kinetic inductance nanowire galvanometer for cryogenic detectors at 4.2 K", arXiv:1709.02640 [cond-mat, physics:physics] (2017).
- <sup>19</sup>L. Krusin-Elbaum, R. L. Greene, F. Holtzberg, A. P. Malozemoff, and Y. Yeshurun, "Direct Measurement of the Temperature-Dependent Magnetic Penetration Depth in Y-Ba-Cu-O Crystals", *Physical Review Letters* **62**, 217–220 (1989).
- <sup>20</sup>D.-X. Chen, C. Navau, N. Del-Valle, and A. Sanchez, "Determination of London penetration depth from ac susceptibility measurements of a square superconducting thin film", *Physica C: Superconductivity* **500**, 9–13 (2014).
- <sup>21</sup>W. H. Henkels and C. J. Kircher, "Penetration depth measurements on type II superconducting films", *IEEE Transactions on Magnetics* **13**, 63–66 (1977).
- <sup>22</sup>B. Langley, S. M. Anlage, R. F. W. Pease, and M. R. Beasley, "Magnetic penetration depth measurements of superconducting thin films by a microstrip resonator technique", *Review of Scientific Instruments* **62**, 1801–1812 (1991).
- <sup>23</sup>J. Bardeen, "Critical Fields and Currents in Superconductors", *Reviews of Modern Physics* **34**, 667–681 (1962).
- <sup>24</sup>K. K. Likharev, "Superconducting weak links", *Reviews of Modern Physics* **51**, 101–159 (1979).
- <sup>25</sup>S. P. Chockalingam, M. Chand, J. Jesudasan, V. Tripathi, and P. Raychaudhuri, "Superconducting properties and Hall effect of epitaxial NbN thin films", *Physical Review B* **77**, 214503 (2008).
- <sup>26</sup>C. P. Bean and J. D. Livingston, "Surface barrier in type-II superconductors", *Physical Review Letters* **12**, 14–16 (1964).

- <sup>27</sup>A. A. B. Brojeny and J. R. Clem, "Self-field effects upon the critical current density of flat superconducting strips", *Superconductor Science and Technology* **18**, 888–895 (2005).
- <sup>28</sup>K. Il'in, M. Siegel, A. Engel, H. Bartolf, A. Schilling, A. Semenov, and H.-W. Huebers, "Current-Induced Critical State in NbN Thin-Film Structures", *Journal of Low Temperature Physics* **151**, 585–590 (2008).
- <sup>29</sup>A. Engel, H. Bartolf, A. Schilling, K. Il'in, M. Siegel, A. Semenov, and H.-W. Hübers, "Temperature- and field-dependence of critical currents in NbN microbridges", *Journal of Physics: Conference Series* **97**, 012152 (2008).
- <sup>30</sup>J. Loudon and P. Midgley, "Imaging flux vortices in type II superconductors with a commercial transmission electron microscope", *Ultramicroscopy* **109**, 700–729 (2009).
- <sup>31</sup>R. B. Dinner, A. P. Robinson, S. C. Wimbush, J. L. MacManus-Driscoll, and M. G. Blamire, "Depairing critical current achieved in superconducting thin films with through-thickness arrays of artificial pinning centers", *Superconductor Science and Technology* **24**, 055017 (2011).
- <sup>32</sup>G. Blatter, M. V. Feigel'man, V. B. Geshkenbein, A. I. Larkin, and V. M. Vinokur, "Vortices in high-temperature superconductors", *Reviews of Modern Physics* **66**, 1125–1388 (1994).
- <sup>33</sup>E. F. Talantsev, A. E. Pantoja, W. P. Crump, and J. L. Tallon, "Current distribution across type II superconducting films: a new vortex-free critical state", *Scientific Reports* **8**, 1716 (2018).
- <sup>34</sup>E. H. Rhoderick and E. M. Wilson, "Current Distribution in Thin Superconducting Films", *Nature* **194**, 1167–1168 (1962).
- <sup>35</sup>E. F. Talantsev, W. P. Crump, and J. L. Tallon, "Universal scaling of the self-field critical current in superconductors: from sub-nanometre to millimetre size", *Scientific Reports* **7**, 10010 (2017).
- <sup>36</sup>L. N. Cooper, "Current Flow in Thin Superconducting Films", in *Proceedings of the VIIth International Conference on Low Temperature Physics* (1961), pp. 416–418.
- <sup>37</sup>P. M. Marcus, "Currents and Fields in a Superconducting Film Carrying a Steady Current", in *Proceedings of the VIIth International Conference on Low Temperature Physics* (1961), pp. 418–420.
- <sup>38</sup>S. Rahbar and E. Hashemizadeh, "A computational approach to the Fredholm Integral Equation of the second kind", in *Proceedings of the World Congress on Engineering*, Vol. 2 (2008), pp. 933–937.
- <sup>39</sup>R. E. Glover and H. T. Coffey, "Critical Currents in Thin Planar Films", *Reviews of Modern Physics* **36**, 299–302 (1964).
- <sup>40</sup>J. R. Clem and V. G. Kogan, "Kinetic impedance and depairing in thin and narrow superconducting films", *Physical Review B* **86**, 174521 (2012).

- <sup>41</sup>F. Tafuri, J. R. Kirtley, D. Born, D. Stornaiuolo, P. G. Medaglia, P. Orgiani, G. Balestrino, and V. G. Kogan, "Dissipation in ultra-thin current-carrying superconducting bridges; evidence for quantum tunneling of Pearl vortices", *Europhysics Letters (EPL)* **73**, 948–954 (2006).
- <sup>42</sup>K. K. Berggren, Q.-Y. Zhao, N. Abebe, M. Chen, P. Ravindran, A. McCaughan, and J. C. Bardin, "A superconducting nanowire can be modeled by using SPICE", *Superconductor Science and Technology* **31**, 055010 (2018).
- <sup>43</sup>Y. T. Yemane, M. J. Sowa, J. Zhang, L. Ju, E. W. Deguns, N. C. Strandwitz, F. B. Prinz, and J. Provine, "Superconducting niobium titanium nitride thin films deposited by plasma-enhanced atomic layer deposition", *Superconductor Science and Technology* **30**, 095010 (2017).
- <sup>44</sup>F. Mercier, S. Coindeau, S. Lay, A. Crisci, M. Benz, T. Encinas, R. Boichot, A. Mantoux, C. Jimenez, F. Weiss, and E. Blanquet, "Niobium nitride thin films deposited by high temperature chemical vapor deposition", *Surface and Coatings Technology* **260**, 126–132 (2014).
- <sup>45</sup>M. S. Wong, W. D. Sproul, X. Chu, and S. A. Barnett, "Reactive magnetron sputter deposition of niobium nitride films", *Journal of Vacuum Science & Technology A: Vacuum, Surfaces, and Films* **11**, 1528–1533 (1993).
- <sup>46</sup>A. E. Dane, A. N. McCaughan, D. Zhu, Q. Zhao, C.-S. Kim, N. Calandri, A. Agarwal, F. Bellei, and K. K. Berggren, "Bias sputtered NbN and superconducting nanowire devices", *Applied Physics Letters* **111**, 122601 (2017).
- <sup>47</sup>A. McCaughan, *CAD layout and GDS geometry creation utilities for photonic and superconducting circuits: amccaugh/phidl*, <https://github.com/amccaugh/phidl> (visited on 09/05/2018).
- <sup>48</sup>J. R. Clem and K. K. Berggren, "Geometry-dependent critical currents in superconducting nanocircuits", *Physical Review B* **84**, 174510 (2011).
- <sup>49</sup>Microchem, *Polymethylglutarimide (PMGI) Resists*, [http://microchem.com/Prod-PMGI\\_LOR.htm](http://microchem.com/Prod-PMGI_LOR.htm) (visited on 09/04/2018).
- <sup>50</sup>M. Colangelo, "Development of resistor process for the fabrication of shunted superconducting nanowire single photon detectors (SNSPD)", M.Sc. thesis (Politecnico di Torino, 2017).
- <sup>51</sup>D. Zhu, "Superconducting nanowire single-photon detectors on aluminum nitride photonic integrated circuits", M.Sc. thesis (Massachusetts Institute of Technology, 2017).
- <sup>52</sup>T. Okada, J. Fujimori, M. Aida, T. Yoshizawa, M. Katsumura, and T. Iida, "Enhanced resolution and groove-width simulation in cold development of ZEP520a", *Journal of Vacuum Science & Technology B, Nanotechnology and Microelectronics: Materials, Processing, Measurement, and Phenomena* **29**, 021604 (2011).

- <sup>53</sup>A. E. Grigorescu and C. W. Hagen, "Resists for sub-20-nm electron beam lithography with a focus on HSQ: state of the art", *Nanotechnology* **20**, 292001 (2009).
- <sup>54</sup>F. Najafi, A. Dane, F. Bellei, Q. Zhao, K. A. Sunter, A. N. McCaughan, and K. K. Berggren, "Fabrication Process Yielding Saturated Nanowire Single-Photon Detectors With 24-ps Jitter", *IEEE Journal of Selected Topics in Quantum Electronics* **21**, 1–7 (2015).
- <sup>55</sup>ZEONREX Electronic Chemicals, *ZEP520A Technical Report*, Apr. 2003, <http://www.nanophys.kth.se/nanophys/facilities/nfl/resists/zep520a-7-2.pdf>.
- <sup>56</sup>S. Bentley, X. Li, D. Moran, and I. Thayne, "Two methods of realising 10nm T-gate lithography", *Microelectronic Engineering* **86**, 1067–1070 (2009).
- <sup>57</sup>Yokogawa Test & Measurement Corporation, *GS200 DC Voltage / Current Source*, <https://tmi.yokogawa.com/solutions/products/generators-sources/programmable-dc-sources/gs200/> (visited on 09/09/2018).
- <sup>58</sup>Lake Shore Cryotronics Inc., *Model CPX Specifications*, <https://www.lakeshore.com/products/cryogenic-probe-stations/model-cpx-cryogenic-probe-station/pages/Specifications.aspx> (visited on 09/04/2018).
- <sup>59</sup>J. R. Taylor, *An introduction to error analysis: the study of uncertainties in physical measurements*, 2nd ed (University Science Books, Sausalito, Calif, 1997).
- <sup>60</sup>Z. Wang, A. Kawakami, Y. Uzawa, and B. Komiyama, "Superconducting properties and crystal structures of single-crystal niobium nitride thin films deposited at ambient substrate temperature", *Journal of Applied Physics* **79**, 7837–7842 (1996).
- <sup>61</sup>H. Bartolf, A. Engel, A. Schilling, K. Il'in, and M. Siegel, "Fabrication of metallic structures with lateral dimensions less than 15nm and  $j_c(T)$ -measurements in NbN micro- and nanobridges", *Physica C: Superconductivity and its Applications* **468**, 793–796 (2008).
- <sup>62</sup>L. N. Bulaevskii, M. J. Graf, C. D. Batista, and V. G. Kogan, "Vortex-induced dissipation in narrow current-biased thin-film superconducting strips", *Physical Review B* **83**, 144526 (2011).
- <sup>63</sup>D. E. Oates, A. C. Anderson, C. C. Chin, J. S. Derov, G. Dresselhaus, and M. S. Dresselhaus, "Surface-impedance measurements of superconducting NbN films", *Physical Review B* **43**, 7655–7663 (1991).
- <sup>64</sup>T. Yamashita, S. Miki, K. Makise, W. Qiu, H. Terai, M. Fujiwara, M. Sasaki, and Z. Wang, "Origin of intrinsic dark count in superconducting nanowire single-photon detectors", *Applied Physics Letters* **99**, 161105 (2011).
- <sup>65</sup>M. S. Hossain, K. Yoshida, K. Kudo, K. Enpuku, and K. Yamafuji, "Enlargement of kinetic inductance of NbN superconducting thin films for device applications", *Japanese Journal of Applied Physics* **31**, 1033–1038 (1992).

- <sup>66</sup>F. Bellei, A. P. Cartwright, A. N. McCaughan, A. E. Dane, F. Najafi, Q. Zhao, and K. K. Berggren, “Free-space-coupled superconducting nanowire single-photon detectors for infrared optical communications”, *Optics Express* **24**, 3248 (2016).
- <sup>67</sup>J. R. Clem, B. Bumble, S. I. Raider, W. J. Gallagher, and Y. C. Shih, “Ambegaokar-Baratoff – Ginzburg-Landau crossover effects on the critical current density of granular superconductors”, *Physical Review B* **35**, 6637–6642 (1987).